Accepted Manuscript

Bioevents and redox conditions around the Cenomanian–Turonian anoxic event in Central Mexico

Fernando Núñez-Useche, Carles Canet, Ricardo Barragán, Pura Alfonso
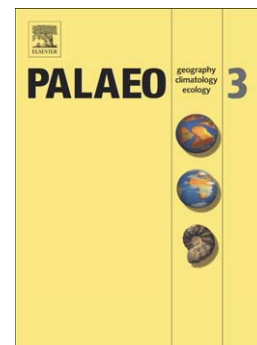
Please cite this article as: Núñez-Useche, Fernando, Canet, Carles, Barragán, Ricardo, Alfonso, Pura, Bioevents and redox conditions around the Cenomanian–Turonian anoxic event in Central Mexico, *Palaeogeography, Palaeoclimatology, Palaeoecology* (2016), doi: 10.1016/j.palaeo.2016.01.035

Bioevents and redox conditions around the Cenomanian–Turonian anoxic event in Central Mexico

Fernando Núñez-Useche[1,2], Carles Canet[2], Ricardo Barragán[3], Pura Alfonso[4]

[1]Posgrado en Ciencias de la Tierra, Universidad Nacional Autónoma de México, Del. Coyoacán, 04510 México D.F., Mexico

[2]Instituto de Geofísica, Universidad Nacional Autónoma de México, Del. Coyoacán, 04510 México D.F., Mexico

[3]Instituto de Geología, Universidad Nacional Autónoma de México, Del. Coyoacán, 04510 México D.F., Mexico

[4]Departament d'Enginyeria Minera i Recursos Naturals, Universitat Politècnica de Catalunya, Av. Bases de Manresa 61−73, 08242 Manresa, Spain

ABSTRACT

The Xilitla section of central Mexico, proto-North Atlantic, is characterized by pelagic sediments enriched in marine organic matter. Using biostratigraphic and radiometric data, it was dated at the latest Cenomanian–earliest Turonian transition. We identified an interval coeval with the turnover of Oceanic Anoxic Event 2, recording the *Heterohelix* shift and the "filament event" for the first time in Mexico. An integral analysis of sedimentary facies, pyrite and geochemical proxies reveals vertically variable redox conditions, with prevailing anoxic to dysoxic bottom waters. Along with phosphorous and manganese depletion, the highest content of total organic carbon and certain redox-sensitive trace elements (RSTEs) is found during part of the anoxic event, confirming more uniform and constant oxygen-depleted conditions. This interval is also characterized by a significant enrichment in biogenic barium and elevated TOC/N_{TOT} ratios, suggesting a link between productivity and anoxia. Sulfur isotope fractionation has a maximum value within the anoxic event, favored by both the increase in the flux of organic matter and

intensified through sulfur recycling. Highly bioturbated beds representing short-lived episodes of oxic conditions are intermittent within the anoxic event, and become more frequent in the early Turonian. This study proposes a model similar to that of modern upwelling regions. High marine productivity controlled organic matter burial and oxygenation at the seafloor, varying between anoxic (laminated facies with small pyrite framboids) and dysoxic conditions (bedding-parallel bioturbated facies with inoceramid bivalves and large pyrite framboids), interrupted by short-term well-oxygenated episodes (thoroughly bioturbated facies with common benthic foraminifera). General low-oxygen conditions led to the formation of glauconite and pyrite (bacterially mediated); the enrichment of redox-sensitive trace elements in sediments such as Cd, Zn, V and Cr scavenged by organic matter and Ni, Mo, Pb, Co and Re by pyrite resulted in Mn and P depletion.

1. INTRODUCTION

Throughout the Mesozoic, several short-lived episodes of marine anoxia caused profound imprints on life and the environment, termed Oceanic Anoxic Events (OAEs; Schlanger and Jenkyns, 1976). The Cenomanian–Turonian anoxic event (OAE 2) is one of the most dramatic episodes of accelerated global change to have occurred throughout the Cretaceous, during a major global sea-level rise. Water column oxygen depletion in the course of this event caused significant faunal turnover, enhancing the deposition of organic-rich sediments leading to a prominent positive carbon isotope excursion (Leckie et al., 2002; Caron et al., 2006; Jiménez Berrocoso et al., 2008; Hetzel et al., 2009; Gambacorta et al., 2015). In addition to affecting the global carbon cycle, the increased delivery of organic carbon to the seafloor drove an expansion of the oxygen minimum zone, elevated trace metal abundance in sediments, and favored high bacterial sulfate reduction

2

(BSR) rates that, in turn, increased sedimentary pyrite burial and led to important modifications in seawater sulfur isotope composition (Coccioni and Luciani, 2004; Denne et al., 2014; Lowery et al., 2014; Poulton et al., 2015; Reolid et al., 2015).

The precise driving mechanisms behind the OAE 2 are still under debate; however, proposed hypotheses for the widespread ocean anoxia/dysoxia include the release of large quantities of CO_2 into the atmosphere through massive submarine volcanic activity in the Caribbean Plateau. Seawater chemistry changed radically due to the introduction of large quantities of sulfate and biolimiting metals that enhanced primary marine productivity (Snow et al., 2005; Trabucho Alexandre et al., 2010). Additionally, the associated CO_2 outgassing favored global warming, thus accelerating the hydrological cycle and increasing continental runoff and nutrient delivery into surface waters, which also contributed to increase productivity. Moreover, enhanced recycling of phosphorous and other nutrients from sediments overlain by anoxic waters has likely been an active mechanism further sustaining marine productivity (Mort et al., 2007; Poulton et al., 2015). While this event is well recorded in the Tethys, Central Atlantic and the Western Interior Seaway (WIS) in North America (e.g., Hetzel et al., 2009; Bomou et al., 2013; Eldrett et al., 2014), it is poorly understood in the Mexican Sea, a key area representing the transition between the WIS and the open ocean.

The Xilitla section of the Tampico-Misantla Basin, central Mexico, contains organic-rich sediments of the Agua Nueva Formation. It offers a good opportunity to study paleoenvironmental response to OAE 2 global perturbation in this particular site of the proto-North Atlantic Basin. In the present study, we present a multi-proxy approach to the stratigraphic section, correlating information from sedimentary facies, biostratigraphy, carbon and sulfur isotopes, and total organic carbon and redox-sensitive trace elements (RSTEs). The goals of this contribution are to (i) identify the bioevents linked to global turnover across the Cenomanian–Turonian (C–T) transition, (ii) provide information illustrating the redox conditions of the depositional environment; (iii) decipher the causes of such conditions and explore their genetic link with OAE 2; and (iv) construct a

3

general depositional model considering the analytical results of the different proxies. This investigation is critical to developing a better understanding of the impact of OAE 2 upon the deposition and preservation of organic matter in the study area.

2.   GEOLOGIC AND PHYSIOGRAPHIC SETTING

The Tampico–Misantla Basin (TMB) is the easternmost paleogeographic feature of a set of basins that once constituted the Cretaceous Mexican Sea along the eastern margin of the proto-North Atlantic Basin (Fig. 1). The basin has a continental basement, and its Jurassic (continental clastic sediments) to Early Cretaceous (basinal carbonates) filling pattern was mainly controlled by sea level changes related to the passive-margin development that resulted from the opening of the proto-Gulf of Mexico (Goldhammer and Johnson, 2001). During the late Cenomanian–early Turonian interval, as a result of the maximum global sea level rise (Hardenbol et al., 1998), the Mexican Sea expanded greatly and connected with the Western Interior Seaway (WIS) and the deep-water pelagic limestone of the Agua Nueva Formation accumulated in the TMB. This event was contemporary with volcanic activity in the western Pacific Mexico province (Goldhammer and Johnson, 2001; Centeno-García et al., 2008). As a consequence of the Sevier and Laramide orogenies and the resulting closure of the Mexican Sea in the Late Cretaceous, the TMB evolved into a flysch-filled foreland basin (Suter, 1984; Morán-Zenteno, 1994). The Xilitla section is situated on the west limb of a syncline fold in the footwall of the Xilitla Thrust (21° 23' 47" N, 98° 59' 88" W, base of the section) (Fig. 1). It is exposed on the northern edge of the village of the same name, along the road to Las Pozas connecting with federal highway 120 (Fig. 1). The continuous sedimentary succession is distributed along four small adjacent artisanal quarries, and comprises 29 m of pelagic sediments from the Agua Nueva Formation. They correspond to limestone with chert intercalated with thin calcareous shale and greenish bentonite horizons. Dark, laminated beds rich in organic matter (total organic carbon, TOC between 1 and 8%) and with well-preserved fossil-fish

4

assemblages, tiny shells of bivalves and pyrite, alternating with bioturbated beds, are reported in different studies (Blanco et al., 2010, 2011; Blanco-Piñón et al., 2008, 2009, 2012, 2014). Without the adequate biostratigraphic control necessary in this type of research, the aforementioned studies considered a C–T age for this unit and highlighted the potential link between the anoxic depositional environment and global OAE 2.

3.   MATERIALS AND METHODS

3.1   *Field and petrographic observations*

The studied section was described and sampled bed-by-bed. Field descriptions focused on the color of the fresh and weathered rock, sedimentary structures, ichnofabric and fossil content. Colors were defined according to the Geological Society of America (GSA) Rock-Color Chart (Goddard et al., 1963). Furthermore, 120 thin sections of calcareous beds were petrographically analyzed under transmitted light microscopy (Olympus BX60) using the nomenclature of Dunham (1962). The microscopic study paid special attention to further descriptions of components and fabric type, as well as the presence/absence of bioturbation and early diagenetic minerals. The degree of bioturbation was described using the index proposed by Taylor and Goldring (1993). Facies are assigned a letter in the oxygen-restricted biofacies (ORB) scheme proposed by Reolid et al. (2010), which is slightly different from that originally presented by Wignall and Hallam (1991) and Wignall (1994). The petrographic analysis of thin sections was also applied in order to semi-quantitatively estimate the abundance of heterohelicids and bivalve filaments. Identification of index species of planktic foraminifera was based on the zonation scheme of Premoli Silva and Sliter (2002). The results of these studies provide information about age, sedimentary features, fossils and mineral composition that constitute the basis for facies characterization and differentiation.

3.2   *U–Pb geochronology*

5

Selected individual homogenous grains were analyzed for U-Pb isotope analysis using Laser Ablation Inductively Coupled Plasma Mass Spectrometry (LA–ICP–MS) composed of a Resonetics M50 workstation coupled with a Thermo X Series II quadrupole ICPMS at the *Centro de Geociencias*, *Universidad Nacional Autónoma de México* (UNAM). Sample preparation and correction of results were performed according to the methodology described by Solari et al. (2009), which produced accuracy better than 0.5% and precision within the range of 2–3% 2σ error. Age was estimated considering the criteria of Jeffries et al. (2003) concerning the age of a single zircon, and of Gehrels et al. (2006) regarding a robust age based on a cluster of three or more zircons with similar ages. All calculations and graphs were made using Isoplot 3.00 by Ludwig (1991).

3.3 *Analysis of pyrite grains*

A statistical study of grain size was applied to pyrite framboids from twenty-two samples in order to assess their size, distribution and content. This task entailed observation of polished sections under a reflected light with an Olympus BX60 microscope. All framboids, contained in two ribbons parallel to the stratigraphic plane and separated between 0.5 and 0.8 mm, were photographed and measured under maximum magnification (100×). For comparison, at least 55 framboids per sample were also measured under a scanning electron microscope (SEM) at the *Instituto de Geología* and the *Instituto de Ciencias del Mar y Limnología* (UNAM) using gold-coated rock chips. Framboid content is reported as the number of framboids per mm^2.

Wavelength dispersive spectrometry (WDS) and energy dispersive X-ray spectroscopy (EDS) analyses were carried out on both diagenetic pyrite framboids >8 µm in diameter with no evidence of overgrowth (disseminated in the matrix and filling burrows) and crystals from laminated pyrite. This analysis was performed on thin, critically point-dried sections coated with a thin layer of gold, using a JEOL JXA-8900XR electron probe microanalyzer (EPMA) (*Instituto de Geofísica,* UNAM) and a model JSM 6300 SEM (*Instituto de Geología,* UNAM). This analysis provides data

concerning the chemical composition of pyrite grains. EDS analysis focused on the content and distribution of carbon, whereas WDS analysis on the content of major and trace elements (Fe, S, V, Ni, Cr, Mo, U and Th).

Pyrite sulfur isotope composition was determined for fourteen grains, which were separated from laminae using a dental drill with a Tungsten Carbide end. These grains are composed of relatively intact pyrite microcrystals and were carefully hand-picked under a binocular microscope; those selected were free from visible sulfur minerals (including barite crystals). The analyses were performed with a Delta C Finnigan MAT continuous flow mass spectrometer, coupled with a TC-EA Carlo Erba 1108 elemental analyzer. Analyses were made following the methodology of Giesemann et al. (1994), at the *Centres Científics i Tecnològics* of the *Universitat de Barcelona* using 0.15–0.20 mg of sample material. Results are expressed using the $\delta^{34}S_{py}$ notation, in permil relative to the VCDT (Vienna Canyon del Diablo Troilite) standard, and have a standard deviation of ±0.2‰.

3.4   Carbonate carbon- and oxygen-isotope data

Carbon and oxygen isotope values on the carbonate fraction of the matrix ($\delta^{13}C_{carb}$ and $\delta^{18}O_{carb}$, respectively) were obtained from sixty samples extracted from micritic matrix of laminated and bioturbated limestone and shaly limestone fragments, with a dental drill (employing a Tungsten Carbide end) and avoiding veins and hydrocarbon impregnations. Orthophosphoric acid was added to about 0.9 mg of each sample at 25 °C and allowed to react for 54 hours under vacuum, following the guidelines of McCrea (1950). The CO_2 released was analyzed with a Thermo Finnigan MAT 253 mass spectrometer coupled with Gas Bench II at the *Laboratorio Universitario de Geoquímica Isotópica* of the *Instituto de Geología* (UNAM). Carbon and oxygen isotope values are reported in permil relative to the VPDB (Vienna Pee Dee Belemnite) standard. Reproducibility of replicate analyses of samples was generally better than 0.2‰ for both carbon and oxygen isotope ratios.

3.5 Whole–rock geochemistry

Fresh limestone and shaly limestone chips of about 1–2 cm in length (free of veinlets, stylolites and hydrocarbons) were collected at a depth of at least 4–6 cm from the exposed surface, in order to avoid the effects of weathering. These were washed with distilled water and dried prior to being powdered with an agate pestle and mortar to < 75 μm. Each sample was separated into aliquots for different whole-rock geochemical analyses.

In order to obtain information relevant to organic carbon content and the origin of organic matter, samples from the three major types of sedimentary facies (laminated and bioturbated calcareous beds) were analyzed through the application of various techniques. Determination of total organic carbon (TOC) was performed by measuring total carbon and total inorganic carbon at the *Laboratorio de Paleoambientes* of the *Instituto de Geología* (UNAM). The measurements were taken using a HiperTOC solid analyzer (Thermo Scientific), which employs an infrared cell to measure the CO_2 produced by combustion. Total carbon concentration was measured by heating 20-40 mg of sample material to 980 °C, and total inorganic carbon was determined by acidifying the sediment with 10% H_3PO_4. TOC content was calculated by subtracting total inorganic carbon from total carbon. Accuracy and precision of both analyses are better than 5%. Total nitrogen (N_{TOT}) was also determined using 2.0 mg of sample material with a CHNS/O Perkin Elmer 2400 series II, mode CHN at the *Laboratorio de Edafología Ambiental* of the *Instituto de Geología* (UNAM). The carrier gas was He, and the combustion and reduction temperatures were 980° and 640 °C, respectively.

Additionally, pyrolysis on samples with TOC values above 1% was performed using a model 6 turbo ROCK-EVAL analyzer, marketed by Vinci Technologies, at the *Laboratorio de Geoquímica y Petrografía Orgánicas* of the *Instituto Mexicano del Petróleo* (IMP). For this analysis, 100 mg of sample material were heated to 300°C in order to release volatile hydrocarbons (S_1). Later, sample pyrolysis was performed at a rate of 25 °C per minute until reaching 600°C to release pyrolytic

8

hydrocarbons (S_2). The CO_2 released was trapped inside a thermal conductivity detector to quantify thermally produced (S_3) organic CO_2 (TOC). The hydrogen index (HI) was obtained by dividing S_2 × 100 by TOC, and the oxygen index (OI) by dividing S_3 × 100 by TOC (Espitalié et al., 1985). These parameters represent the amount of hydrogen and oxygen relative to the amount of organic carbon present in a sample, respectively.

Concentrations of major and trace elements were determined for twenty-nine samples from laminated and moderately bioturbated beds distributed along the entire stratigraphic column. These analyses were carried out at Activation Laboratories Ltd. (Actlabs) in Canada, through Inductively Coupled Plasma/Optical Emission Spectrometry (ICP-OES; Varian 735) and Inductively Coupled Plasma Mass Spectrometry (ICP-MS; Perkin Elmer Sciex ELAN 9000), after the digestion of 1.0 g of sample material using four different acids (HF, $HClO_4$, HNO_3 and HCl) (Package code Ultratrace 6). For evaluation of the analytical performance of the method, standards GXR-1, GXR-2, GXR-6, SAR-M, DNC-1 and SBC-1 of the United States Geological Survey, and DH-1a from the Canada Centre for Mineral and Energy Technology were analyzed at the beginning and end of each batch of samples. Percentages of the relative standard deviation were consistently below 10%, as corroborated by standards and analysis of replicate samples.

All elemental concentrations were normalized to aluminum content in order to remove the effect of variable terrigenous input, as well as to differentiate the authigenic contribution of redox-sensitive trace elements (RSTEs) (Calvert and Pedersen, 1993; Brumsack., 2006; Tribovillard et al., 2006; Reolid et al., 2015). Aluminum is commonly of detrital origin, and is usually immobile during biological and diagenetic processes (e.g., Calvert and Pedersen, 1993). In addition, to compare the relative enrichment of RSTEs, we calculated the enrichment factor (EF) for a given element (X) relative to average shale value (Wedepohl, 1971): $EF_{element} = (X/Al)_{sample} / (X/Al)_{average shale}$. An EF>3 represents detectable authigenic enrichment of the element over average shale concentration, and an EF>10 represents a moderate to strong degree of authigenic enrichment (e.g. Tribovillard et al., 2006).

Biogenic barium (Ba$_{bio}$; a proxy for bio-productivity) was calculated using the normalized approach proposed by Dymond et al., (1992): Ba$_{bio}$ = Ba$_{total}$ - (Al × (Ba/Al)$_{detrit}$. In this equation, the Ba/Al$_{detrit}$ represents the Ba/Al ratio of the detrital fraction. As the composition of the detrital source was not available, we used the global average ratio (0.0037) proposed by Reitz et al. (2004).

Nine samples for X-ray powder diffraction analysis were ground with an agate pestle and mortar to <75 μm and mounted in aluminum holders for determining mineral composition. A Shimadzu XRD-6000 X-ray diffractometer equipped with a Cu tube and graphite monochromator was used at the XRD laboratory of the *Instituto de Geología*, *Universidad Nacional Autónoma de México* (UNAM). The analyses were applied to randomly oriented samples, using the measurement range (2θ) of 4 to 70° at a speed of 1°/min.

All analytical and calculated data presented are available electronically in Supplementary Appendix A.

4. RESULTS

4.1 Age of the Xilitla section

Previous studies close to the town of Xilitla (Blanco et al., 2011; Blanco-Piñón, 2008, 2014) have reported an age spanning the C–T transition for the Agua Nueva Formation, on account of the joint presence of the distinctive planktic foraminifera *Rotalipora cuhsmani* and the bivalve *Inoceramus labiatus*. Nonetheless, these studies do not provide a biostratigraphic framework that would allow a more precise constraint on the time of deposition. In this study, we use U–Pb zircon geochronology and bioevents to give more accurate information in this regard.

Zircons from sample Az (bed 11; at 1.7 m) (Figs. 2 and 3) give an age that varies between 89 and 100 Ma. The youngest concordant zircon age is 89 ± 0.7 Ma; however, an even more concordant zircon provides an age of 93 ± 1.0 Ma. The calculated age (TuffZirc algorithm) for a group of fourteen zircons is 95 ± 0.3 Ma. Based on the mean age of the seventeen most concordant

zircons, an age of 94.1±1.6 Ma was obtained. Considering these data, the latter age is regarded as being more robust.

Four important bioevents that are commonly recognized within the latest Cenomanian–earliest Turonian transition (Keller et al., 2004; Coccioni and Luciani, 2004; Caron et al., 2006; Robaszynski et al., 2010; Negra et al., 2011; Kędzierski et al., 2012; Bomou et al., 2013; Denne et al., 2014; Lowery et al., 2014; Reolid et al., 2015) were identified within the section studied (Fig. 2). From base to top they correspond to:

(i)   The last occurrence of *Rotalipora cushmani* (Morrow) (top of the *Rotalipora cushmani* Total Range Zone), identified in bed 17 (at 2.8 m).

(ii) The *Heterohelix* shift, characterized by a peak in heterohelicid abundance (40-50% of allochems), identified in bed 29 (at 5.1 m).

(iii) The so-called "filament event", characterized by a peak in filament accumulation (30-40% of the allochems), identified in beds 93–95 (from 15.8 to 16.2 m). Filaments are translucent grains about 10–900 μm in length and 0.3-2 μm wide, and match known thin-shelled juvenile pelagic bivalves. Blanco-Piñón et al. (2014) had already reported the presence of these filaments in the Agua Nueva Formation of the Xilitla area.

(iv) The first occurrence of *Helvetoglobotruncana helvetica* (Bolli) (base of the *Helvetoglobotruncana helvetica* Total Range Zone), identified in bed 106 (at 17.2 m).

It is noteworthy that the identification of the *Heterohelix* shift and the filament event is the first documentation of their presence in Mexico. Taking these four bioevents into account, the lower 2.8 m of the studied section belong to the top of the *R. Cushmani* Total Range Zone, whereas the *Whiteinella archaeocretacea* Partial Range Zone spans from 2.8 to 17.2 m and the *H. helvetica* Total Range Zone starts at 17.2 m and extends above the top of the section (Fig. 2). The filament event occurs in other sections just above the C–T boundary, before or coeval with the first Turonian

index ammonite *Watinoceras* (Caron et al., 2006; Negra et al., 2011). Building upon this consideration, we place the C–T boundary below bed 93 (at 15.8 m) in the studied section (Fig. 2).

4.2 Facies description and occurrence

At the field scale, the Xilitla section consists of an interbedded sequence of calcareous rocks and bentonites. The former corresponds to fissile and shaly limestone displaying various shades of black and gray (N1 to N8) on fresh cuts, and dark yellowish orange (10YR 6/6) to pale yellowish orange (10YR 8/6) on weathered surfaces (Fig. 4A–B). These beds are essentially tabular and vary in thickness from 2 to 42 cm. They frequently contain layers (with a pinch-and-swell structure, Fig. 4C) and nodules of flint parallel to bedding, with various dimensions (centimeter-scale) and lenticular to irregular shape. Sets of fractures and stylolites with oil stain are common at some calcareous levels. On the other hand, bentonite beds are light olive gray (5Y 6/1) on fresh cuts (Fig. 4D) and moderate reddish orange on weathered surfaces (10R 6/6), vary in thickness from 2 to 20 cm, and are common from 10 m to the top of the section. Thick successions of bentonite beds can be observed between 12 and 16 m (Fig. 2). The most remarkable lithologic feature of the Xilitla section is the common presence of laminated beds containing pyrite (Fig. 4E–F), fish remains and inoceramid bilvalves, interspersed with bioturbated layers (Fig. 4F). Both field and petrographic observations allow for the discrimination of various redox facies, deposited in a pelagic marine environment and which are described below.

4.2.1 Facies F1. Dark laminated/non-bioturbated mudstone/wackestone rich in pyrite and glauconite

This facies consists of dark gray (N3) to black (N1), thinly laminated beds with a low bioturbation index (0–1) (weak to absent bioturbation) (Figs. 4E–F and 5A–B). Pyrite laminae from less than 1 mm to 8 mm thick alternate with thinner layers of calcareous material (Fig. 5A–B).

12

Pyrite occurs less commonly as nodules, including the variety called "*Pyrite Sun*" (Fig. 5C), which consists of a flat disc shape constituted of radiating, acicular crystals. This facies also contains common well-preserved fish remains (Fig. 5D–E) and scarce ammonites (Fig. 5F). Microscopically, this facies may be divided in two subfacies:

-*Subfacies F1A*: Mudstone and bioclastic wackestone with planar laminated (Fig. 6A) to anisotropic fabric (Fig. 6B); abundant planktic foraminifera (Fig. 6A–D); common fish remains (Fig. 6B) and bivalve fragments (Fig. 6C); rare ostracods, and echinoderm fragments. Micro-lamination is more accentuated in limestone and is defined by laminae with parallel boundaries, sometimes wavy, that differ in color and internal composition (Fig. 6A). Darker laminae are medium dark gray (N4) to dark gray (N3) micritic layers high in organic matter and clay concentration and contain few scattered fossils, whereas lighter laminae are fossiliferous. Millimetric laminae of bentonite, alternating with calcareous/argillaceous laminae, are rarely observed within the upper 10 m of the section. Subfacies F1A contains abundant disseminated pyrite framboids (Fig. 7A and E), in addition to frequent glauconite as infilling of foraminiferal tests or as cement within intergranular porosity (Fig. 6D). It is the most dominant type of facies in the whole section, although, it is more continuously present within the lowest 9 m (top *R. Cushmani*–middle *W. archaeocretacea* zones) (Fig. 2).

-*Subfacies F1B*: This subfacies consists of wackestone with a grayish yellow (5Y 8/4) argillaceous matrix yielding abundant radiolarians, common fish remains, and is almost barren of planktic foraminifera (Fig. 6E). It shows some degree of anisotropic fabric, along with several stages of silicification and dolomitization that dim the presence of framboidal pyrite and glauconite. Subfacies occur in relatively short, intermittent episodes (discrete beds of 10–20 cm), solely between 10 and 16 m (middle *W. archaeocretacea*–base *H. helvetica* zones) (Fig. 2).

4.2.2 Facies F2. Poor to moderately bioturbated wackestone/packstone

It consists of medium gray (N5) to medium light gray (N6) laminated beds with a bioturbation index of 2–3 (poorly to moderately bioturbated). Burrows are mainly bedding-parallel (Fig. 5G–H) and mostly include *Planolites* (Fig. 5I) and *Chondrites* (Fig. 5J). Pyrite is disseminated, as laminae, or as burrow infill (Fig. 5G). Inoceramid bivalve shells (Fig. 5K-L) and fish remains (Fig. 5K) are frequent. Ripple marks are regularly present on the top surface of beds (Fig. 5M). Facies F2 is the second most dominant type of facies, occurring regularly throughout the stratigraphic section (Fig. 2)

Microscopically, this facies is related to silty bioclastic wackestone and packstone with a yellowish gray (5Y 8/1) micritic matrix (Fig. 6F-G). Planktic foraminifera are the dominant skeletal allochems, and are commonly recrystallized and densely packed. Bivalve filaments are common, and benthic foraminifera and ostracods are rarely present. Lamination is moderately preserved, and usually interrupted by burrows with irregular outlines (Fig. 6F-G). Disseminated pyrite corresponds mainly to framboids (Fig. 7B-D and F). Glauconite is less common than in facies F1, and occurs mainly as cement infilling intergranular porosity.

Some scattered, straight to gently curved filaments (thin-shelled pelagic bivalves) are regularly present in both facies F1 and F2 between 0 and 18 m. An interval with a significant accumulation of these filaments (increase in 30-40%) can be observed in beds 93–95 (15.8–16.2 m) (filament event; Fig. 2).

4.2.3 Facies F3. Highly bioturbated, light-colored wackestone/packstone

This facies consists of thoroughly bioturbated limestone (bioturbation index mostly between 4 and 5), with no evidence of lamination or pyrite. Its distinguishing feature is the presence of vertical and oblique burrows with different cross-cutting relationships (Figs. 4F and 5N–Q).

Based on the constrast between burrows fills and the host sediment, this facies can be subdivided into two types: (i) light-on-dark (LOD) bioturbated facies, characterized by abundant trace fossils in a burrow-mottled and dark matrix (Fig. 5N); and (ii) dark-on-light (DOL) bioturbated facies with

common overlapping burrows (Fig. 5O–P). Small *Chondrites* burrows and large *Zoophycos*-like trace fossils (Fig. 5N) occur in both patterns, as well as vertical and oblique burrows (Fig. 5O–Q). Facies F3 occur as short, isolated events within the lowest 16 m of the studied section, but become more common within the upper 12 m (especially in the uppermost 6 m) (*H. Helvetica* Zone) (Fig. 2).

Microscopic observations show that this facies consists of wackestone and packstone with a moderate yellow (5Y 7/6) micritic matrix containing abundant planktic foraminifera and common benthic foraminifera (Fig. 6H–I). These grains are highly recrystallized and can be packed. Lamination is not evident, and samples exhibit a mottled appearance characterized by vertical burrows (Fig. 6I). Disseminated pyrite and glauconite are absent in this facies.

4.3   *Pyrite framboid size distribution and content*

Disseminated pyrite morphology in this study includes: (i) spherical framboids that consist of microcrystal pyrite aggregates, commonly with intercrystal porosity; (ii) irregular anhedral to subhedral masses; and (iii) euhedral pyrite grains. Of these, the framboids are the most common (Fig. 7). Preliminary observations of unpolished rock chips, under SEM, revealed the presence of different microcrystal size, form and organization inside the framboids (Fig. 7C–F). Although the morphology and size of the majority is clearly preserved, thus conducive to measurement, some of them have been partially or totally recrystallized (with minor internal porosity or as a pyrite spheroid) or show evidence of secondary growth.

Pyrite framboids only occur in facies F1 and F2, mainly within the lowest 11 m of the section. Their stratigraphic distribution and main statistical parameters of size and content are listed in Table 1 and depicted in Fig. 8. Although the size of framboids varies slightly from sample to sample, they are generally rather small, with mean diameters of between 5.0 μm in bed 30 (facies F1) and 7.6 μm in bed 152 (facies F2). The small-sized framboid population is recorded in beds 30, 35, 131 and 194

(all composed of facies F1), whereas framboids with diameters >10 µm are more common in the upper part of the stratigraphic section, mainly in beds 152 and 187 (both constituted of facies F2), and bed 161 (facies F1). The highest framboid content occurs mainly in beds of facies F1 with values of 1213 per mm^2 (bed 210), 620 per mm^2 (bed 1) and 541 per mm^2 (bed 62). Of the analyzed beds included in facies F2, only bed 10 has a significant content of 558 per mm^2. The minimum number of framboids occurs in facies F2 with a value of 70 per mm^2 (beds 65 and 187).

4.4   Stable isotopes and organic matter characterization

Carbon isotope values vary between -1.9 and +1.6‰ (Fig. 9 and Appendix B). The most striking feature of the $\delta^{13}C_{carb}$ curve is a distinct negative shift of 2.7‰ from 9.3 to 11.2, followed by a return to baseline values. Oxygen isotope data ($\delta^{18}O_{carb}$; Appendix B) show considerable variation across the whole stratigraphy, fluctuating between -3.4‰ and -6.5‰ (-4.4‰ on average).

The TOC content fluctuates between 0.32 and 3.32%, with most of the samples rich in organic carbon recorded within the lowest 9 m of the section (top *R. Cushmani*–middle *W. archaeocretacea* zones) (Fig. 10). In general, facies F3 shows low TOC values (consistently below 1%), while facies F1 and F2 have a higher content (ranging from 1 to 3.32%). The analyzed samples have a relatively high hydrogen index (HI; 276–468 mg H/g TOC) and low oxygen index (OI; 8–39 mg O/g TOC) values (Fig. 11). Total nitrogen concentration (N_{TOT}) ranges between 0.04 and 0.06%, leading to TOC/N_{TOT} ratios between 22.5 and 55.3 (Fig. 10). Low and high values of HI, OI and N_{TOT} are randomly distributed among sedimentary facies.

4.5   Major and trace elements

Al-normalized RSTEs contents are compared to TOC and total S (S_{TOT}) contents (Fig. 10 and Appendix B). In general, Cd, V, Zn and Cr display a decreasing trend with higher ratios in the lowest 9 m (top *R. Cushmani*–middle *W. archaeocretacea* zones) of the section, where TOC reach

elevated values. Conversely, Ni, Co, Pb and Mo present a flat pattern with minor peaks at different levels. In detail, the interval between 1 and 9 m records maximum peaks of Cu/Al (164.84×10^{-4}) at 1.4 m; V/Al (404.08×10^{-4}) at 2.5m; Fe/Al (0.96) and Zn/Al (426.61×10^{-4}) at 2.8 m; and U/Al (9.81×10^{-4}) at 4.8 m. This interval also shows a significant increase of Cr/Al (118.16×10^{-4}), as well as a moderate increase of Ni/Al (66.94×10^{-4}) at 2.5m. Several pronounced peaks of Ba/Al with values of up to 438.46×10^{-4} can also be observed within the lower 9 m, where Mn/Al is consistently low (down to 104.86×10^{-4}). The interval between 9 and 29 m (middle *W. archaeocretacea–H. helvetica* zones) records moderate increases of Cd/Al (2.78×10^{-4}) and Zn/Al (341.06×10^{-4}) at 15.4 m; Cr/Al (90.68×10^{-4}), Ag/Al (1.73×10^{-4}) and Cu/Al (123.78×10^{-4}) at 17.1 m; and Cr/Al (153.69×10^{-4}), Co/Al (15.85×10^{-4}), Ag/Al (0.57×10^{-4}) and Cu/Al (64.62×10^{-4}) at 22.6 m.

Otherwise, S, Fe/Al, Co/Al, Pb/Al and Mo/Al exhibit a relatively flat pattern. Raw concentration of S presents dramatic increases at 10.1 m (7.43%) and 28.7 m (8.73%). In the latter stratigraphic position, the maximum peaks also occur for Fe/Al (18.24), Ni/Al (240.73×10^{-4}), Co/Al (28.54×10^{-4}), Pb/Al (57.07×10^{-4}), Ag/Al (2.12×10^{-4}), Mo/Al (40.24×10^{-4}) and Re/Al (0.154×10^{-4}), in addition to moderate to slight peaks of V/Al (270.73×10^{-4}) and Cr/Al (43.41×10^{-4}). The P/Al ratio exhibits low values in the lower 9 m of the section, with values between 0.03 and 0.09, and afterward increases slowly showing pronounced peaks at 22.6 m (0.12), 27.5 m (0.12), and 28.7 m (0.11).

The calculated EFs for trace elements are shown in Fig. 12. Analyzed samples are consistently enriched in RSTEs compared to the average shale. The largest mean EFs are recorded for Cd (167.06), Ag (69.89), Re (37.22), Mo (16.80), Zn (10.31), V (8.72), U (8.07) and P (7.29). Fe, Cr, Ni, Co, Pb, Cu, and Mn record moderate to low EFs (mean EFs between 2.22 and 7.93). Note that mean EFs of Cd, Zn, V, Cr, Cu, U and Ba from the lowest 9 m are higher than those of the whole section.

Observations of thin rock sections and XRD analyses reveal that the detrital fraction of analyzed samples does not exceed 40%; indeed, they consist mainly of marine carbonate (65–92%, average

17

84.7%). This indicates that the Ba/Al ratio of Reitz et al. (2004) is valid for calculating reliable biogenic barium concentration. Accordingly, the Ba_{bio} content fluctuates between 472.53 (at 6.9 m, bed 39) and 1.9 ppm (at 5.4 m, bed 30) (with an average of 110.34 ppm) (Fig. 10).

4.6   *Elemental and sulfur isotope composition of pyrite grains*

The results of EDS and WDS analysis confirm that sulfides present in the studied sediments are pyrite. Under the SEM, a low density matrix occurs between pyrite microcrystals and/or enveloping the surface of the entire framboids (in both those disseminated in the matrix and those infilling burrows) (Fig. 13). EDS analysis on framboids reveals that such interstitial material is enriched in carbon, compared to pyrite crystals. Otherwise, the elemental data acquired through WDS analysis (Table 2) show that laminated and framboidal pyrite both contain significant quantities of Mo (~4500–6000 ppm) and lesser amounts of Ni (~200–400 ppm) and U (~220–2280 ppm). Regarding the sulfur isotope composition, $\delta^{34}S_{py}$ values of the analyzed grains (composed of pyrite microcrystals) are consistently negative, ranging from -5.2‰ (bed 106) to -51.2‰ (bed 13) (Fig. 14). The $\delta^{34}S_{py}$ profile displays an increasing trend from -51.2 ‰ at 1.9 m to -5.1‰ at 14.3 m.

5.   DISCUSSION

5.1   *Correlations based on bioevents and definition of the OAE 2 time-equivalent interval*

The OAE 2 time-equivalent interval is commonly delimited by a large positive carbon isotope excursion (with three distinctive peaks), both in marine inorganic carbonate (2–4‰) and organic matter (up to 6‰), interpreted to be the result of enhanced burial of ^{12}C-enriched organic matter (Keller et al., 2004; Caron et al., 2006; Bomou et al., 2013) (Fig. 9). However, in the $\delta^{13}C_{carb}$ profile (Fig. 9 and Appendix B) from the Xilitla section there is not a truly defined positive shift. Overall, the $\delta^{13}C_{carb}$ values are unusually lower in comparison to the Cretaceous $\delta^{13}C_{carb}$ database (Leckie et al., 2002; Föllmi, 2012). They are depleted by more than 1.5–3‰ compared to contemporaneous

18

marine calcite. Likewise, the $\delta^{18}O_{carb}$ values (Appendix B) are also low compared to those found in Cretaceous pelagic sediments (Clarke and Jenkyns, 1999). This difference can be the result of both diagenetic effects and local conditions. For instance, alteration of the $\delta^{13}C$ is possibly linked to early diagenetic modification, as a result of the transfer of isotopically light carbon from bacterial degradation of organic matter to carbonate cement. Diagenetic effects during burial (pore water interaction and/or dissolution and recrystallization) can be also considered, given the recrystallization of skeletal allochems.

Major biological changes across the C–T transition are also a useful tool to trace the OAE 2 time-equivalent facies (Coccioni and Luciani, 2004; Caron et al., 2006; Bomou et al., 2013; Reolid et al., 2015) (Fig. 9). Among planktic foraminifera, the onset of the global turnover associated with the anoxic event occurs mostly below the last occurrence of *R. Cushmani,* marking the disappearance of planktic foraminifera of complex morphology and with a longer and deeper life-cycle (K-species like the rotaliporids), which have adapted to oligotrophic stable nutrient levels in deep and intermediate waters. They disappeared due to the oceanic perturbation of oxygen levels within the *W. archaeocretacea* Zone, conversely favoring the proliferation of species with a short and shallow life-cycle (r-selected species such as the heterohelicids and whiteinellids). The first occurrence of *H. helvetica* marks the reappearance of complex keeled morphotypes (K-selected species), thus reflecting the return to stable nutrient conditions and the end of the anoxic event.

In the studied section, within the *W. archaeocretacea* Zone, both the *Heterohelix* shift (bed 29, at 5.1 m) (Fig. 2) and the "filament event" (bed 93–9, 15.8–16.2 m) (Fig. 2) highlight environmental conditions of great stress during the turnover related to OAE 2. The rapid rise in the abundance of heterohelicids (surface-dweller opportunists) is associated to the better adaptation of these organisms to sudden environmental change (temperature, salinity, nutrient level), and commonly indicates a drop in water column oxygenation (e.g., Caron et al., 2006; Reolid et al., 2015). Otherwise, the abundance of filaments is interpreted as the result of the mass mortality of planktonic bivalve larvae (e.g., Caron et al., 2006; Kędzierski et al.,2012; Bomou et al., 2013)

19

and/or the product of disintegration of pelagic bivalves during high-energy events (Negra et al., 2011). They are related to heightened marine productivity and oxygen-deficient water masses. Both bioevents have also been observed worldwide in a similar biostratigraphic position in the Western Interior Seaway (Pueblo section-GSSP, Caron et al., 2006; Atascosa and Karnes cores, Denne et al., 2014), and in the Tethys (Gongzha section-Tibet, Bomou et al., 2013; Rybie section-Poland; Kędzierski et al., 2012; wadi Bahloul-Tunisia, Caron et al., 2006 and Reolid et al., 2015) (Fig. 9). For the first time in Mexico, the record of the *Heterohelix* shift and the filament event is the expression of an effective connection between the Mexican Sea and the aforementioned oceanic basins during the C–T transition. Furthermore, the occurrence of the "filament event" below the base of the *H. helvetica* Zone supports the use of this bioevent as a global stratigraphic marker preceding the restoration of keeled planktonic foraminifera, in opposition to what is suggested by Desmares et al. (2007).

Considering the connection between the aforementioned bioevents and the main peaks in the $\delta^{13}C$ curve defining the anoxic event, the OAE 2 time-equivalent interval in the Xilitla section can be constrained to the lowermost 15.8 m (Fig. 9). This position for the OAE 2 interval is also supported by the robust radiometric age estimated from bentonite Az (94.1 ± 1.6 Ma) (Fig. 3). This result is compatible with the astronomically recalibrated radiometric age of 93.90 ± 0.15 Ma for the C–T boundary proposed by Meyers et al. (2012) (Fig. 9).

5.2   Assessing redox conditions

5.2.1 Interpretation of sedimentary facies

   -Interpretation of facies F1: The lack of bioturbation (Figs. 5A–B and 6A–B) and absence of benthic foraminifera are consistent with anoxic bottom-water conditions (ORB-A; Reolid et al., 2010). Such conditions precluded burrowers and allowed the preservation of abundant disarticulated fish parts (Figs. 5D–E and 6B) that settled to the sediment from oxygenated upper water layers. The

millimetre-scale fine lamination observed in this facies (Figs. 5A–B and 6A) implies deposition in a low-energy environment. The differences in laminae color and content reflect minor fluctuations in sedimentary conditions in the TMB. For instance, the planktonic-rich laminae may reflect short periods of high productivity conditions that sustained the proliferation of calcareous zooplankton. Currently, these blooms in foraminiferal productivity have been observed in certain areas of the Mediterranean (Rigual-Hernández et al., 2012) and North Atlantic Basin (Salmon et al., 2015), where they are associated with seasonal rise in sea surface temperature and nutrient conditions.

The radiolarian–rich beds in the middle part of the section (subfacies F1B) (Figs. 2 and 6E) fit in with the predominance of these organisms in other black shales representing the OAE 2, commonly interpreted as the regional renewal of nutrient-rich waters (Coccioni and Luciani, 2004; Caron et al., 2006; Kędzierski et al., 2012; Gambacorta et al., 2015). Such blooms of organisms with silica skeletons also supported ocean acidification during OAE 2, due to an increased uptake of CO_2 derived from massive volcanic eruptions of the Caribbean Plateau (Gebhardt et al., 2010; Du vivier, 2015a). Under these conditions, planktic foraminifera biomass diminished due to low calcium carbonate availability; radiolarian, less affected by acidification, competed more efficiently and flourished. Considering that subfacies F1B is spatially and temporally associated with the thick successions of bentonite (Fig. 2), a local factor that may have accounted for the silica supply and probably enhanced seawater acidification and selective radiolarian proliferation was volcanic ash-fall in the TMB. It has been demonstrated that fall-out of volcanic ash in the ocean may induce a reduction of the surface water pH, which affects planktonic calcifying organisms (e.g., Cobianchi et al., 2015).

-Interpretation of facies F2: The poor-to-moderate degree of bioturbation of facies F2, coupled with the presence of very few benthic foraminifera, suggests that this facies accumulated under dysoxic oxygen levels (ORB-B of Reolid et al., 2010). Dominance of horizontal burrows disrupting the original lamination (Figs. 5G–I and 6F–G), as well as absence of the vertical, suggests that

21

favorable oxygen conditions at the sediment-water interface allowed organism colonization and that anoxic conditions prevailed within the lower sediment layers. A striking feature of this facies, which further reflects a slight concentration of oxygen at the seafloor, is the common presence of inoceramid shells (Fig. 5K–L). These bivalves flourished under dysoxic bottom-water conditions in several mid-Cretaceous basins (Caron et al., 2006; Jiménez Berrocoso et al., 2008; Ifrim et al., 2011; Lowery et al., 2014). Ripple marks (Fig. 5M) associated with some beds provide evidence of periodic seafloor ventilation by bottom currents.

A high concentration of bivalve filaments in sediments, as observed in facies F1 and F2 (Fig. 2), is thought to be linked to episodes of high marine productivity (Caron et al., 2006; Kędzierski et al., 2012; Bomou et al., 2013). The presence of disseminated framboidal pyrite (Fig. 7) and glauconite (filling primary porosity) (Fig. 6D) in both facies also points towards reducing environments, in which these minerals formed as a syngenetic-early diagenetic phase in the iron reduction zone of the oxic-anoxic interface (e.g., Wilkin et al., 1996; Lowery et al., 2014; Bond et al., 2015).

-Interpretation of facies F3: The composite ichnofabric of this facies (Figs 5N–Q and 6I) indicates intense activity of organisms both at the seafloor surface and within the sediment, under relatively well-oxygenated conditions. Bottom waters with high oxygen concentrations are also suggested by the common presence of benthic foraminifera (Fig. 6H–I). Facies F3 is similar to ORB-D of the model of Reolid et al. (2010). An oxic environment may have heightened aerobic remineralization of organic matter, a process that commonly inhibits pyrite formation (e.g Bond and Wignall, 2010) and accounts for the lack of pyrite in this facies.

From facies F1 to F3, there is a clear progressive increase in the availability of oxygen at the bottom of the water column. Indeed, a higher TOC content in facies F1 and F2 (>0.51%) than in facies F3 (<1%) supports this interpretation. From observing the vertical distribution of said facies (Fig. 2), it is evident that oxygen deficiency was more uniform within the lowest 9 m of the section,

during the lower part of the OAE 2 interval. Afterward, the bottom-water redox conditions became more variable and oxygen increased progressively during relatively short and intermittent episodes, mainly in the post-OAE 2 interval.

5.2.2 Pyrite framboid size and content distribution

Many studies have shown that the size, distribution and content of pyrite framboids are regulated by bottom-water redox conditions, controlled by the position of the oxic-anoxic interface relative to the sediment-water interface (Wilkin et al., 1996; Bond and Wignall, 2010; Núñez-Useche et al., 2015). Oxygen-depleted (dysoxic) bottom waters, where the oxic-anoxic interface is close to the sediment-water interface, favor the formation of diagenetic framboids (>6 μm in diameter) at the sediment-water interface and within the sediment. Under more oxygen-restricted conditions, the oxic-anoxic interface moves upward and abundant syngenetic framboids are formed in the anoxic water column. Since they rapidly sink to the seafloor, syngenetic framboids are smaller (4-6 μm in diameter) and less variable in size than diagenetic framboids. Euxinic conditions (free H_2S) also produce populations of tiny syngenetic framboids (3-5 μm in diameter) within a narrow size range.

Mean vs. standard deviation plot of pyrite framboid data from Xilitla (Fig. 8 and Table 1) shows a distinction between anoxic and dysoxic conditions, quite consistent with the facies interpretation: framboids of anoxic facies F1 are smaller and less variable in size (mostly syngenetic; suggesting more oxygen-depleted conditions) than those of dysoxic facies F2 (mostly diagenetic).

Although most pyrite framboids in both facies indicate poorly-oxygenated bottom waters, all samples from facies F1 contain tiny framboids (<5 μm in diameter) - with a content higher than 18% - that may have resulted from intermittent euxinicity. This is more evident for samples 30, 131 and 194, which fall close to the euxinic field and exhibit a content of tiny framboids exceeding 40%. Considering the low content of framboids in these samples, their framboid populations might reflect short-lived pulses of euxinia superimposed on longer term anoxic conditions, which may result in a time-averaged framboid population typical of anoxic environments (e.g., Bond and

23

Wignall, 2010). The content of framboidal pyrite (Fig. 8 and Table 1) is less indicative of oxygen conditions. Many samples from dysoxic facies F2 have a greater framboid content than those from anoxic facies F1. This is probably because the bioturbated fabric of facies F2 favored upward diffusion of H_2S from underlying sediments, in which bacterial sulfate reduction (BSR) continued but iron limited pyrite formation, thus prompting framboid formation somewhat independently from redox conditions. This phenomenon has been invoked previously for sulfur excess in dysoxic facies with low TOC (e.g., Algeo and Maynard, 2004).

5.2.3 Redox control of trace element enrichment

Under oxygen-depleted bottom waters, certain RSTEs are less soluble and preferentially transferred from the water column into the sediment. Conversely, Mn is reduced to soluble forms (Mn^{2+} or $MnCl^+$) that are not readily taken up by organic matter; it diffuses upward out of sediment or from the sediment-water interface (Calvert and Pedersen, 1993; Canet et al., 2004; Algeo and Maynard, 2004; Tribovillard et al., 2006).

RSTEs/Al ratios of sediments from Xilitla are consistently above those of average shale (Fig. 10 and Appendix B). Their EFs values include the mean of the C–T black shales (Brumsack, 2006) and those from modern sediments underlying anoxic environments (Calvert and Pedersen, 1993) (Fig. 12). Several Al-normalized RSTEs ratios covary with TOC (R_{Cd}=0.72, R_{Zn} =0.68, R_V =0.67, and R_{Cr}=0.61) and S_{TOT} (R_{Ni}=0.73, R_{Mo}=0.72, R_{Pb}=0.68, R_{Co}=0.67, and R_{Re}=0.67) (Table 3), suggesting that trace elements were mainly fixed in organic and authigenic Fe-sulfide phases. These correlations indicate that, despite the diagenetic overprint of the carbonate fraction affecting the $\delta^{13}C$ record, great alteration of the trace element data is ruled out. This is because in organic-rich sediments, the carbonate fraction exerts lesser control on the whole rock trace elements content than the organic and sulfide fractions do (Abanda and Hannigan, 2006; Xu et al., 2012).

Both correlation patterns agree with the known geochemical behavior of RSTEs under low oxygen conditions (Calvert and Pedersen, 1993; Algeo and Maynard, 2004; Brumsack, 2006; Tribovillard et al., 2006). In the sediments studied, the peaks of Cd/Al and Zn/Al (elements generally incorporated into marine plankton biomass) may record episodes of intensive primary production. Correlation of Al-normalized concentrations of V and Cr with TOC and not with S_{TOT} reflect the preferential incorporation of these elements into organic matter. Conversely, correlation of Mo/Al, Co/Al, Ni/Al and Re/Al with S_{TOT} reflect the higher degree of pyritization of these trace elements. The presence of Mo and Ni in both laminated and framboidal pyrite (Table 2) corroborates their incorporation into pyrite (probably taken up in solid solution), and supports reduced conditions in pore waters under which these elements are absorbed by pyrite. Although Pb is commonly removed as an independent sulfide phase rather than in solid solution in pyrite, high levels of Pb pyritization are also reported in anoxic-sulfidic sediments.

Worthy of note is that the RSTE data do not allow differentiation between anoxic facies F1 and dysoxic facies F2. This is because under regular re-oxygenation of the bottom waters, RSTEs behavior is less predictable and they are less consistent as indicators of oxygen levels (e.g, Algeo and Maynard, 2004). Despite this, higher mean EFs for Cd, Zn, V, Cr, Cu and U (Fig. 12), along with the lowest Mn/Al concentration (Fig. 10) and a negative TOC–Mn correlation (R= -0.1) within the lowest 9 m of the section, indicate that more severe and constant oxygen deficiency prevailed during deposition of this stratigraphic interval. From 9–10 m upward, concurrent slight to moderate increases in different RSTEs point to short-lived episodes of low oxygen conditions. Nevertheless, the overall decrease in TOC and certain Al-normalized RSTEs content (Fig. 10) suggests that oxygen deficiency was less severe and more variable within this interval. This interpretation is supported by the gradual increase of the Mn/Al ratio between 10 and 19.8 m (Fig. 10).

Besides local redox conditions, we suggest an important event controlling the RSTEs distribution patterns in the organic-rich sediments from Xilitla. The higher RSTEs concentrations

within the lowest 9 m of the section seem to indicate the introduction of large amounts of trace metals (e.g., Co, Cu, Zn, Se, V, Mo) into the ocean, a phenomenon associated with the submarine volcanism of the Caribbean Plateau, which commenced between 95 and 92 Ma (Snow and Duncan, 2001; Leckie et al., 2002; Snow et al., 2005; Trabucho Alexandre et al., 2010). This is in agreement with the synchronous increase in unradiogenic seawater-osmium at 94.44 ± 0.14 and 94.28 ± 0.25 Ma (close to the OAE 2 onset) found by Du vivier et al. (2015b) in proto-Pacific sections, linked to the basaltic eruptions of said plateau. Accordingly, the decrease trend in certain RSTEs (Cd, V, Zn, Cr and, and to a lesser extent, Cu, U and Re) (Fig. 10 and Appendix B), similar to the one found in other oxic and anoxic sediments (Elrick et al., 2009, Bomou et al., 2013; Eldrett et al., 2014), may reflect the gradual global drawdown of the trace metal reservoir due to widespread deposition of organic-rich sediments in the Tethys and proto-North Atlantic during OAE 2.

To summarize,, our sedimentary, pyrite framboid and geochemical data indicate more permanent reducing environments within the lowest 9 m of the section, likely reflecting oxygen deficient conditions associated with OAE 2, superimposed to the anoxic/dysoxic bottom-water regime inherent to the TMB. Such conditions are comparable to those reported for northern Mexico (Duque-Botero et al., 2009) and Demerara Rise (southern North Atlantic; Hetzel et al., 2009; Trabucho Alexandre et al., 2010), where anoxia was intense. This suggests that the Xilitla section placed within the core of an oxygen-minimum zone. However, these conditions contrast with the oxygenated regime within OAE 2 found in the northern Tethyan pelagic zone (Chrummflueschlucht section; Westermann et al., 2010), the Gamba-Tingri Basin (Gongzha section; Bomou et al., 2013), and in some areas of the Western Interior Seaway (Shell Iona-1 core; Eldrett et al., 2014). Within this poorly-oxygenated regime associated with OAE 2, there were episodes of intermittent oxic conditions reflected by the regular presence of thoroughly bioturbated beds with common benthic foraminifera (facies F3). This indicates a more dynamic benthic environment related to fluctuations of the oxygen-minimum zone. Similar intermittent suboxic conditions have also been documented

26

in the Tarfaya Basin (Kuhnt et al., 2009), the Silesian Basin (Rybie section; Uchman et al., 2013), and in the Central Tunisian Platform (the Oued Bahloul section; Reolid et al., 2015). These variable OAE 2 redox regimes, observed worldwide, point towards strong local influence upon both oxygen conditions and the accumulation of organic-rich sediments in marine basins.

From 9 m upward in the sequence, oxygen deficiency was less severe and more variable, and was controlled by local redox conditions. Oxygen-depleted conditions during the early Turonian have been also reported for southern and northern Mexico during the deposition of the Mexcala Formation (Guerrero-Morelos Platform; Hernández-Romano et al., 1997; Elrick et al., 2009) and the Indidura Formation (Parras Basin; Duque-Botero et al., 2009), respectively. Therefore, regional control of redox conditions during the early Turonian is suggested for this part of the proto-North Atlantic Basin, possibly associated with the intermittent permanence of a weaker oxygen-minimum zone.

5.3   *Sea-level variation*

A major global sea-level rise is known to have occurred during the C–T transition (Hardenbol et al., 1998). In the context of this eustatic fluctuation, the filament event is related to an interval close to the end of the transgressive interval, heralding the transition to normal marine conditions (Negra et al., 2011; Kędzierski et al., 2012). In the Xilitla section, no significant stratigraphic features constrain the extent of said transgressive phase; however, considering the position of the filament event, the transgressive phase could be attributed to the lower part of the section. High sea-level conditions for this interval matches more uniform oxygen-depleted conditions that favored organic-rich sediment formation, mainly in the lowermost 9 m. Above this bioevent, the abundance of limestone beds progressively increases upward within the section. This limestone-dominated interval may reflect a long-term decrease in detrital influx linked to the global sea-level change, such as is observed at Pueblo (USA), Eastbourne (UK) and Ghonza (China) (Bomou et al., 2013).

5.4 Link between marine productivity and anoxia: geochemical evidence

5.4.1 Biogenic barium

Barium is an important tracer of marine productivity (Dymond et al., 1992; Tribovillard et al., 2006; Hetzel et al., 2009). In organic-rich sediments underlying areas of high productivity, bio-induced formation of barite ($BaSO_4$) occurred within organic particles in reducing environments. Intense bacterial sulfate reduction (BSR) may cause sulfate depletion and mobilization of Ba (Dymond et al., 1992); however, the highly negative pyrite $\delta^{34}S$ values from Xilitla suggest that such did not occur in the sediments studied. Therefore, Ba can be reasonably used as a proxy for productivity. Fig. 12 shows a moderate enrichment of Ba in relation to the average shale and comparable to the C–T mean values (Brumsack, 2006). This is indicative of fertile water masses. Since Ba content can be influenced by other sources (e.g., detrital aluminosilicates, hydrothermal precipitates, secretion by benthic organisms) (Dymond et al., 1992), a more reliable evaluation of productivity is achieved using biogenic barium (Ba_{bio}) (Fig. 10). The Ba_{bio} content represents between 3.8 and 91% (63.1% in average) of the Ba total. Therefore, a considerable part of the Ba total is composed of biogenic barium, confirming high productivity. As shown in Fig. 10, both Ba/Al and Ba_{bio} are relatively enriched in the lowest 9 m, thus indicating recurrent intensification of productivity during the deposition of this interval.

5.4.2 Phosphorus content

Phosphorous is an important biolimiting nutrient modulating marine productivity (Tribovillard et al., 2006; Bomou et al., 2013). Dissolved P delivery to the ocean, mostly by continental runoff, is carried to the seafloor by organic matter, clay particles and manganese oxyhydroxides. Under reducing conditions, P diffuses upward from the sediment and returns to the water column, increasing primary productivity (e.g., Mort et al., 2007). Fig. 10 shows a clear enrichment of P compared to average shale in the Agua Nueva Formation that points towards high productivity, analogue to modern coastal upwelling areas in Peru (Böning et al., 2004) and Namibia (Brumsack.,

2006). The minor enrichment in P within the lowermost 9 m suggests partial loss of P linked to more uniform oxygen-depleted conditions. This scenario fits that observed for basins of the Tethys and Atlantic during OAE 2, where anoxia increased P remobilization from sediments to sustain productivity (Mort et al., 2007; Hetzel et al., 2009; Poulton et al., 2015). P availability in this part of the proto-North Atlantic Basin may also have been controlled by both a climate change toward more arid conditions and a long-term sea-level rise, decreasing continental biogeochemical weathering rates, as is observed in Tethyan and Atlantic sections (Bomou et al., 2013).

5.4.3 Elevated TOC/N$_{TOT}$ ratios

In the pseudo-van Krevelen-type diagram (Fig. 11), analyzed samples fall into fields of type I (algal) and type II (algal/microbial) organic matter. This marine origin is not consistent with the obtained TOC/N$_{TOT}$ values (22–55), suggesting a terrestrial source (TOC/N$_{TOT}$ >20; Meyers et al., 2006). Nonetheless, similar unusual TOC/N$_{TOT}$ ratios have also been reported for marine organic matter deposited under areas of high productivity. For instance, values between 10 and 22 were measured by Bouloubassi et al. (1999) in the Mediterranean sapropels. Most of the black shales deposited during mid-Cretaceous OAEs display values of between 25 and 50 (e.g., Meyers et al., 2006). Thus, TOC/N$_{TOT}$ ratios obtained in this study fit highly eutrophic conditions. These anomalous values are a result of the loss of nitrogen during oxygen stress periods linked to high productivity (e.g., Twichell et al., 2002; Van Mooy et al., 2002).

Remarkably, marine productivity was higher within the lowest 9 m, where there were more stable and severe anoxic/dysoxic conditions. This supports a positive feedback loop among high productivity, deposition of organic matter, and oxygen depleted conditions - at least during part of the OAE 2 (Mort et al., 2007; Hetzel et al., 2009; Lowery et al., 2014; Reolid et al., 2015). Based on the regular presence of volcanic ash, we suggest that there was a link between local volcanic input and high productivity. Ash particles can induce natural fertilization by supplying large amounts of bio-available Fe to the ocean (Duggen et al., 2010; Langmann et al., 2010). However, since

bentonite beds are rare in the lowest 9 m (Fig. 2), we suggest that the increase in nutrient conditions was mainly driven by the release of biolimiting elements (Fe and P) into the global ocean, triggered by the coeval volcanic eruptions of the Caribbean Plateau (Snow et al., 2005; Trabucho Alexandre et al., 2010).

5.5 Control of bacterial sulfate reduction and sulfate availability on the sulfur isotope record

The $\delta^{34}S_{py}$ curve from the Xilitla section displays an increasing trend from -51.2‰ (bed 13) to -5.2‰ (bed 106) during and immediately after OAE 2 (Fig. 14). This trend is similar to that found in Demerara Rise (Site 1258; Hetzel et al., 2009), the Western Interior Seaway (Portland Core; Adams et al., 2010), and in shelf sediments from Tarfaya (Core S57; Poulton et al., 2015). In all cases, the $\delta^{34}S_{py}$ reaches a minimum value within the anoxic event and gradually returns to higher values afterwards (Fig. 14). This similarity supports a common mechanism driving the global sedimentary sulfur isotope signal during OAE 2. According to Adams et al. (2010), the sulfur isotope record during the anoxic event was greatly influenced by more availability of seawater sulfate concentration, prompted by the release of sulfur by massive volcanism that progressively declined. Under anoxic conditions, sulfate-reducing bacteria obtain energy by oxidizing organic compounds while reducing marine sulfate to hydrogen sulfide, preferentially incorporating ^{32}S. Therefore, higher sulfate levels during this event must favored a greater fractionation of sulfur through bacterial sulfate reduction (BSR), resulting in lighter $\delta^{34}S$ pyrite.

Interestingly, the Xilitla section shows a minimum $\delta^{34}S_{py}$ value within OAE 2 - quite isotopically lighter compared to that of the aforementioned sites (Fig. 14). Taking the sulfur isotope composition of C–T marine sulfate to be between +17 and +21‰ (average around +19‰; Paytan et al., 2004), and assuming that bottom waters and/or pore waters in sediments were derived from coeval open marine waters, then an overall sulfur isotope fractionation of 26.2 to 72.2‰ during OAE 2 is estimated for the Xilitla section (Fig. 14). In some cases, these values match those found in

laboratories by BSR of 4 to 46‰ (Ohmoto et al., 1990; Canfield, 2001). However, higher values can be explained only through an additional fractionation of the sulfide pool during the oxidative phase of the sulfur cycle, in which oxidation of bacterial HS⁻ to elemental S or other intermediate oxidized S species is followed by the bacterial disproportionation into isotopically lighter sulfide and heavier sulfate (Habicht and Canfield, 1997; Passier et al., 1997). This process has been utilized by Passier et al. (1997) to explain fractionation values of 57.9 to 70.2‰ in the eastern Mediterranean sapropels.

In either case, the large sulfur fractionation in the studied section hints of a dramatic increase in relative seawater sulfate concentration in the TMB during the anoxic event. This increase could be the result of both (i) the compelling variable redox conditions causing increased diffusion of sulfate to lower sediment layers through bioturbation during dysoxic periods, and (ii) bottom currents (as evidenced by ripple marks; Fig. 5M) that contributed to the replenishment of the sulfate reservoir through the mixing of sediment and ambient waters. Both bioturbation and bottom currents might provide the O_2 required for the oxidation of primary pyrite and sulfur recycling. The decrease in sulfur fractionation through the anoxic event in the Xilitla section (Fig. 14) is apparently linked to a decline in burial efficiency of organic matter. This is evident from the inverse relationship between $\delta^{34}S_{py}$ and TOC values observed in the lowermost 18 m. However, after this, $\delta^{34}S_{py}$ values become lighter in the *H. helvetica* Zone in spite of moderate TOC concentration. This return to lighter values is an isotope signature not observed in other sites (Fig. 14), and implies a different mechanism that, once again, contributed to the increase in sulfate concentration and the extent of sulfur fractionation by BSR.

Evidence of bacterial activity in the TMB is confirmed by EDS analysis, revealing the presence of a carbon-rich matrix between microcrystals, like a capsule homogeneously coating the outer surface of both individual microcrystals and pyrite framboids (Fig. 13). This envelope can be interpreted as a remnant of the organic material that constituted an original bacterial biofilm, providing the structural framework for the clustering of pyrite microcrystals According to several

31

research projects, this carbon-rich component is mainly produced by extracellular bacterial polysaccharides and is stretched during framboid maturation (e.g., Rickard, 2012).

5.6   *Depositional model*

The multiproxy approach applied here shows that the organic-rich sediments of the Agua Nueva Formation display vertically variable sedimentary facies, and predominantly provides evidence of oxygen-depleted conditions in bottom waters interrupted by punctuated, short-lived oxic episodes. Based on the correlation of several proxies, we proposed a model to explain these episodically dysaerobic conditions.

As shown in Fig. 15, a layer of oxygen-depleted seawater developed just at the seafloor, as a consequence of oxygen consumption by decaying marine organic matter from high biologically productive surface waters; this is similar to the scenario encountered in modern coastal upwelling areas. Above this layer, there was greater oxygen availability, coinciding with the presence of abundant fish and ammonite remains. Variations in total primary production controlled the supply of organic matter to the seafloor, thus producing redox variations in bottom waters mostly from anoxic (facies F1) to dysoxic (facies F2) conditions. Under anoxic conditions (Fig. 15A), the oxic-anoxic interface was located above the sediment-water interface. Such conditions precluded colonization by benthic fauna and preserved finely-laminated fabric. Diagenetic and syngenetic pyrite framboid formation through BSR took place at both the anoxic water column and the sediment-water interface. The increase in oxygen content of bottom waters caused the deepening of the oxic-anoxic interface, which placed at the sediment-water interface or just beneath it (Fig. 15B). Therefore, dysoxic conditions developed close to the sediment-water interface and within the uppermost sediments, whereas anoxic conditions persisted in pore waters within the lower sediments. Sporadic bottom currents favored mixing with oxygenated water and contributed to sustaining dysoxic conditions. This scenario allowed the colonization of the seafloor by inoceramid

bivalves and other low-oxygen tolerant benthic taxa (including benthic foraminifera) that burrowed into the sediment and disrupted lamination. Pyrite framboids were diagenetically formed - mainly in the uppermost sediment. Influx of H_2S from the underlying sediments, provided by BSR and favored by the bioturbated fabric, may have stimulated additional diagenetic framboid formation. In the model, overall low oxygen levels (anoxic and dysoxic) promoted glauconite formation and the scavenging of trace elements and their incorporation to sediments. Whereas Cd, Zn, V and Cr were mainly fixed in organic matter and Ni, Mo, Pb, Co and Re were scavenged by pyrite, Mn and P diffused out of the sediments. Biogenic barium also enriched sediments linked to organic matter decay. Bioturbation and bottom currents played an important role in enhancing the diffusion of sulfate to lower sediment for BSR and providing the O_2 for sulfur recycling.

During periods of low productivity and low export of organic matter from the marine surface, the oxic-anoxic interface deepened below the sediment-water interface (Fig. 15C). This caused oxic conditions at both the seafloor and the upper sediments, which allowed intense bioturbation and the establishment of benthic foraminifera, as well as anoxic/dysoxic conditions in the lower sediments.

6.   CONCLUSIONS

Biostratigraphic and radiometric data reveal that the Xilitla section spans the latest Cenomanian–earliest Turonian interval. Four important global bioevents, which from base to top are (i) the last occurrence of *Rotalipora cushmani*, (ii) the *Heterohelix* shift, (iii) the filament event, and (iv) the first occurrence of *Helvetoglobotruncana helvetica* (Bolli), mark the biotic turnover associated with oxygen-depleted conditions during OAE 2 in the Tampico–Misantla Basin. The occurrence of these bioevents suggests inter-ocean connections of this part of the Proto-North Atlantic with the Tethys Sea and Western Interior Seaway.

According to the constructed model, high marine productivity is associated with organic matter burial and oxygen depletion in the Tampico–Misantla Basin, analogous to that occurring in modern

coastal upwelling areas. Fluctuations in primary production controlled bottom-water oxygen conditions at the seafloor, which remained mostly oxygen-deficient and were interrupted by punctuated, short-lived oxic events (episodically dysaerobic).

The regular presence of the facies of anoxic settings, the higher enrichment in TOC and selected RSTEs, and the depletion in Mn and P, suggest that more constant and severe oxygen deficiency occurred within the lowest 9 m of the studied section, during part of OAE 2. Similar conditions have been found in central and southern Tethys; however, they contrast with oxygenated bottom waters observed in part of the Western Interior Seaway and northern Tethyan margin. This points to local mechanisms operating in different parts of the global ocean, producing dissimilar redox conditions during OAE 2. As indicated by the more constant occurrence of well-oxygenated facies, from 9 m upward oxygen deficiency was less severe; TOC and RSTE decrease, and Mn and P increase.

Marine productivity was triggered by nutrient fertilization from intrabasinal volcanic ash-fall. However, higher eutrophic conditions in the lowest 9 m of the section may have been reinforced by P recycling from sediments, along with the release of biolimiting metals into the global ocean during coeval massive volcanic eruptions of the Caribbean Plateau. This submarine volcanism apparently influenced trace element availability and burial in sediments: higher within the lowest 9 m, and declining progressively afterward.

A positive trend in the stable sulfur isotope curve with minimum values within OAE 2 indicates that highest isotope fractionation was related to organic matter burial. This pattern is similar to the one observed at other sites, thus suggesting globally controlled changes in the overall sulfur cycle, likely from the release of sulfur by massive volcanism. Locally, a greater availability of both seawater sulfate concentration in lower sediments (as a result of bioturbation and/or bottom currents) and organic matter (favored by high primary production) enhanced BSR and increased the extent of fractionation during pyrite formation. Sulfur recycling favored by variable redox conditions account for the highly negative $\delta^{34}S$ values for pyrite.

Acknowledgments

REFERENCES

Abanda, P. A., Hannigan, R.E., 2006. Effect of diagenesis on trace element partitioning in shales. Chemical Geology 230, 42–59.

Adams DD, Hurtgen MT, Sageman B.B., 2010. Volcanic triggering of a biogeochemical cascade during Oceanic Anoxic Event 2. Nature Geoscience 3, 201–204.

Algeo, Th.J., Maynard, J.B., 2004. Trace-element behavior and redox facies in core shales of Upper Pennsylvanian Kansas-type cyclothems. Chemical Geology 206, 289–318.

Blanco, A., Zavala, F.J., Hernández-Ávila, J., Maurrasse, F., Duque-Botero, F., Ramírez-Cardona, M., 2010. Microbial preservation in sedimentary pyrite from Cretaceous organic-matter-rich carbonate mudstone: A preliminary report. Lunar and Planetary Science Conference, 2487.

Blanco, A., Maurrasse, F. J., Duque, F., Delgado, A., 2011. Anoxic–dysoxic–oxic conditions in the Cenomanian Agua Nueva Formation (Upper Cretaceous) in central Mexico, and their relation to Oceanic Anoxic Event 2 (OAE 2). Geological Society of America, Abstracts with Programs, 43, 421.

Blanco-Piñón, A., Maurrasse, F.J-M.R., Rojas-León, A., Duque-Botero, F., 2008. Cyanobacteria/Foraminifera Association from Anoxic/Dysoxic Beds of the Agua Nueva Formation (Upper Cretaceous - Cenomanian/Turonian) at Xilitla, San Luis Potosi, Central Mexico (summary), Eos Trans of the American Geophysical Union, The meeting of the Americas: Fort Lauderdale, FL, USA, 89 (23). Jt. Assem. Suppl., Abstract pp. 24A-04.

Blanco-Piñón A., Zavala-Diaz de la Serna, F.J., Hernandez-Avila, J., Maurrasse, F., Duque-Botero, F., 2009. Microscopic bioforms in Pyritic Layers from the Cenomanian/Turonian (Upper Cretaceous) Agua Nueva Formation, Xilitla, Central Mexico: A Preliminary Description. Geological Society of America, Abstracts with Programs 41, p. 82.

Blanco-Piñón, A., Ángeles-Trigueros, S.A., Hernández-Ávila J., Zavala-Díaz de la Serna, F.J., 2012. SEM imaging of biostructures in Upper Cretaceous sedimentary pyrite: an astrobiological approach. Geological Society of America. Abstracts with Programs, 44, p. 75.

Blanco-Piñón, A., Maurrasse, F.J.-M.R., Zavala Díaz-de la Serna, F.J., López-Doncel, R.A., Ángeles-Trigueros, S.A., Hernández-Avila, J., Juárez Arriaga, E., 2014. Evidencias petrográficas de estructuras de origen algal/bacteriano en carbonatos de la Formación Agua Nueva (Cenomaniano/Turoniano: Cretácico Superior) en Xilitla, S. L. P. México Central. Boletín de la Sociedad Geológica Mexicana 66, 397–412.

Bomou, B., Adatte, T., Tantawy, T., Mort., H., Fleitmann, D., Huang, Y., Föllmi, K.B., 2013. The expression of the Cenomanian–Turonian oceanic anoxic event in Tibet. Palaeogeography, Palaeoclimatology, Palaeoecology 369, 466–481.

Bond, D.P.G., Wignall, P.B., 2010. Pyrite framboid study of marine Permian–Triassic boundary sections: A complex anoxic event and its relationship to contemporaneous mass extinction. Geological Society of America Bulletin 122, 1265–1279.

Böning, P., Brumsack, H.J., Böttcher, M.E., Schnetger, B., Kriete, C., Kallmeyer, J., Borchers, S.L., 2004. Geochemistry of Peruvian near-surface sediments. Geochimica et Cosmochimica Acta, 68(21), 4429–4451.

Brumsack, H.-J., 2006. The trace metal content of recent organic carbon-rich sediments: implications for Cretaceous black shale formation. Palaeogeography, Palaeoclimatology, Palaeoecology 232, 344–361.

Calvert, S.E., Pedersen, T.F., 1993. Geochemistry of Recent oxic and anoxic marine sediments: Implications for the geological record. Marine Geology 113, 67–88.

Canet, C., Alfonso, P., Melgarejo, J.C., Belyatsky, B.V., 2004. Geochemical evidences of sedimentary-exhalative origin of the shale-hosted PGE–Ag–Au–Zn–Cu occurrences of the Prades Mountains (Catalonia, Spain): trace-element abundances and Sm–Nd isotopes. Journal of Geochemical Exploration 82, 17–33.

Canfield, D.E., 2001. Isotope fractionation by natural populations of sulfate-reducing bacteria. Geochimica et Cosmochimica Acta 65, 1117–1124.

Caron, M., Dall'Agnolo, S., Accarie, H., Barrera, E., Kauffman, E.G., Amédro, F., Robaszynski, F., 2006. High-resolution stratigraphy of the Cenomanian–Turonian boundary interval at Pueblo (USA) and wadi Bahloul (Tunisia): stable isotope and bioevents correlation. Geobios 39, 171–200.

Centeno-García, E., Guerrero-Suastegui, M., Talavera-Mendoza, O., 2008. The Guerrero Composite Terrane of western Mexico: Collision and subsequent rifting in a supra-subduction zone. Geological Society of America Special Paper 436, 279–308.

Clarke, L.J., Jenkyns, H.C., 1999. New oxygen isotope evidence for long-term Cretaceous climatic change in the Southern Hemisphere. Geology 27, 699–702.

Cobianchi, M., Mancin, N., Lupi, C., Bordiga, M., Bostock, H. C., 2015. Effects of oceanic circulation and volcanic ash-fall on calcite dissolution in bathyal sediments from the SW Pacific Ocean over the last 550ka.Palaeogeography, Palaeoclimatology, Palaeoecology, 429, 72–82.

Coccioni, R., Luciani, V., 2004. Planktonic foraminifera and environmental changes across the Bonarelli Event (OAE2, latest Cenomanian) in its type area: a highresolution study from the Tethyan reference Bottaccione section (Gubbio, central Italy). Journal of Foraminiferal Research, 34, 109–129.

Denne, R. A., Hinote, R. E., Breyer, J. A., Kosanke, T. H., Lees, J. A., Engelhardt-Moore, N., Spaw, F.M., Tur, N., 2014. The Cenomanian–Turonian Eagle Ford Group of South Texas: insights on timing and paleoceanographic conditions from geochemistry and micropaleontologic analyses. Palaeogeography, Palaeoclimatology, Palaeoecology, 413, 2–28.

Desmares, D., Grosheny, D., Beaudoin, B., Gardin, S., Gauthier-Lafaye, F., 2007. High resolution stratigraphic record constrained by volcanic ash beds at the CenomanianeTuronian boundary in the Western Interior Basin, USA. Cretaceous Research 28, 561–582.

Dunham, R.J., 1962. Classification of carbonate rocks according to depositional textures. In: Ham, W.E. (Ed.), Classification of carbonate rocks a Symposium. American Association of Petroleum Geologists Memoir 1, 108–121.

Duque-Botero, F., Maurrasse, F.J-M-R., Hickey-Vargas, R., Melinte, M., Jaffe, R., Lopez-Oliva, J.G., 2009. Microspheroids accumulation and geochemistry of an anoxic basin of the Cenomanian/Turonian: The record of the Indidura Formation, NE Mexico. Geologic Problem Solving with Microfossils: A Volume in Honor of Garry D. Jones. Society for Sedimentary Geology, Society of Sedimentary Geology Special Publication 93, 171–186.

Du Vivier, A.D.C., Jacobson, A.D., Lehn, G.O., Selby, D., Hurtgen, M.T., & Sageman, B.B. 2015a. Ca isotope stratigraphy across the Cenomanian–Turonian OAE 2: Links between volcanism, seawater geochemistry, and the carbonate fractionation factor. Earth and Planetary Science Letters, 416, 121-131.

Du Vivier, A.D.C., Selby, D., Condon, D.J., Takashima, R., Nishi, H, 2015b. Pacific ^{187}Os/^{188}Os isotope chemistry and U–Pb geochronology: Synchroneity of global Os isotope change across OAE 2. Earth and Planetary Science Letters, 428, 204–216.

Dymond, J., Suess, E., Lyle, M., 1992. Barium in Deep-Sea Sediment: A Geochemical Proxy for Paleoproductivity. Paleoceanography 7, 163–181.

Elrick, M., Molina-Garza, R., Duncan, R., Snow L., 2009. C-isotope stratigraphy and paleoenvironmental changes across OAE 2 (mid-Cretaceous) from shallow-water platform carbonates of southern Mexico. Earth and Planetary Science Letters 277, 295–306.

Eldrett, J.S., Minisini, D., Bergman, S.C., 2014. Decoupling of the carbon cycle during Ocean Anoxic Event 2. Geology 42, 567-570.

Espitalié, J., Deroo, G., Marquis, F., 1985. La pyrolyse Rock-Eval et ses applications. Revue de l'Institut français du pétrole, 40, 563–579.

Gambacorta, G., Jenkyns, H.C., Russo, F., Tsikos, H., Wilson, P.A., Faucher, G., Erba, E., 2015. Carbon-and oxygen-isotope records of mid-Cretaceous Tethyan pelagic sequences from the Umbria–Marche and Belluno Basins (Italy). Newsletters on Stratigraphy, 48(3), 299–323.

Gebhardt, H., Friedrich, O., Schenk, B., Fox, L., Hart, M., Wagreich, M., 2010. Paleoceanographic changes at the northern Tethyan margin during the Cenomanian–Turonian Oceanic Anoxic Event (OAE-2). Marine Micropaleontology, 77(1), 25–45.

Gehrels, G., Valencia, V., Pullen, A., 2006. Detrital zircon geochronology by laser ablation multicollector ICPMS at the Arizona LaserChron Center. In: Olszewski, T. (Ed.), Geochronology: Emergging opportunities. Paleontological Society Papers 12, 67–76.

Giesemann, A., Jäger, H.J., Norman, A.L., Krouse, H.R., Brand, W.A., 1994. Online Sulfur-Isotope Determination Using an Elemental Analyzer Coupled to a Mass Spectrometer. Analytical Chemistry 66, 2816–2819.

Goddard, E.N., Trask, P.D., De Ford, R.K., Rove, O.N., Singewald, J.T., Overbeck, R.M., 1963. Rock-Color Chart. Distributed by the Geological Society of America, New York,16 pp.

Goldhammer, R., Johnson, C., 2001. Middle Jurassic–Upper Cretaceous Paleogeographic Evolution and Sequence-stratigraphic Framework of the Northwest Gulf of Mexico Rim. The Western Gulf of Mexico Basin: tectonics, sedimentary basins, and petroleum systems. American Association of Petroleum Geologists Memoir 75, 45–81.

Habicht, K.S., Canfield, D.E., 1997. Sulfur isotope fractionation during bacterial sulfate reduction in organic-rich sediments. Geochimica et Cosmochimica Acta 61, 5351–5361.

Hardenbol, J., Thierry, J., Farley, M.B., de Graciansky, P.C., Vail, P.P., 1998. Mesozoic and Cenozoic sequence chronostratigraphic framework of European basins. In: de Graciansky, P.C., Hardenbol, J., Jacquin, T., Vail, P.P. (Eds.), Mesozoic and Cenozoic Sequence Stratigraphy of European Basins. society of economic paleontologists and mineralogists Special Publication 60, 3–13.

Hernández-Romano, U., Aguilera-Franco, N., Martínez-Medrano, M., Barceló-Duarte, J., 1997. Guerrero-Morelos Platform drowning at the Cenomanian–Turonian boundary, Huitziltepec area, Guerrero State, southern Mexico. Cretaceous Research 18, 661–686.

Hetzel, A., Böttcher, M.E., Wortmann, U.G., Brumsack, H.-J., 2009. Paleo-redox conditions during OAE 2 reflected in Demerara Rise sediment geochemistry (ODP Leg 207). Palaeogeography, Palaeoclimatology, Palaeoecology 273, 302–328.

Ifrim, C., Götz, S., Stinnesbeck, W., 2011. Fluctuations of the oxygen minimum zone at the end of Oceanic Anoxic Event 2 reflected by benthic and planktic fossils. Geology 39, 1043–1046.

Jeffries, T., Fernández-Suárez, J., Corfu, F., Gutiérrez-Alonso, G., 2003. Advances in U-Pb geochronology using a frequecy quintupled Nd:YAG based laser ablation system (lambda=213 nm) and quadrupole based ICP-MS. Journal of Analytical Atomic Spectrometry 18, 847–855

Jiménez Berrocoso, Á., MacLeod, K.G., Calvert, S.E., Elorza, J., 2008. Bottom water anoxia, inoceramid colonization, and benthopelagic coupling during black shale deposition on Demerara Rise (Late Cretaceous western tropical North Atlantic). Paleoceanography, 23, PA3212.

Kędzierski, M., Machaniec, E., Rodríguez-Tovar, F.J., Uchman, A., 2012. Bio-events, foraminiferal and nannofossil biostratigraphy of the Cenomanian/Turonian boundary interval in the Subsilesian Nappe, Rybie section, Polish Carpathians. Cretaceous Research 35, 181–198.

Keller, G., Berner, Z., Adatte, T., Stueben, D., 2004. Cenomanian–Turonian and δ^{13}C, and δ^{18}O, sea level and salinity variations at Pueblo, Colorado. Palaeogeography, Palaeoclimatology, Palaeoecology 211, 19–43.

Kuhnt, W., Holbourn, A., Gale, A., Chellai, E., and Kennedy, W.J., 2009, Cenomanian sequence stratigraphy and sea-level in the Tarfaya Basin (SW Morocco). Geological Society of America Bulletin 1695–1710.

Langmann, B., Zakšsek, K., Hort, M., Duggen, S., 2010. Volcanic ash as fertiliser for the surface ocean. Atmospheric Chemistry and Physics Discussions 10, 711–734.

Leckie, R.M., Bralower, T.J., Cashman, R., 2002. Oceanic anoxic events and plankton evolution: Biotic response to tectonic forcing during the mid-Cretaceous. Paleoceanography 17, 13–1 to 13–29.

Lowery, C. M., Corbett, M. J., Leckie, R. M., Watkins, D., Romero, A. M., Pramudito, A., 2014. Foraminiferal and nannofossil paleoecology and paleoceanography of the Cenomanian–Turonian Eagle Ford Shale of southern Texas. Palaeogeography, Palaeoclimatology, Palaeoecology, 413, 49–65.

Ludwig, K.R., 1991. A plotting and regression program for radiogenic-isotope data; version 2.53. U.S. Geological Survey Open-File Microsoft excel. Berkeley Geochronlogical Center Special Publication 4a.

McCrea, J.M., 1950. On the Isotopic Chemistry of Carbonates and a Paleotemperature Scale. The Journal of Chemical Physics 18, 849–857.

Meyers, P.A., Bernasconi, S.M., Forster, A., 2006. Origins and accumulation of organic matter in expanded Albian to Santonian black shale sequences on the Demerara Rise, South American margin. Organic Geochemistry 37, 1816–1830.

Meyers, S.R., Siewert, S.E., Singer, B.S., Sageman, B.B., Condon, D.J., Obradovich, J.D., Jicha, B,R., Sawyer, D.A., 2012. Intercalibration of radioisotopic and astrochronologic time scales for the Cenomanian-Turonian boundary interval, Western Interior Basin, USA. Geology, 40(1), 7–10.

Morán-Zenteno, D., 1994. The Geology of the Mexican Republic: AAPG. Studies in Geology 39, p. 160.

Mort, H.P., Adatte, T., Föllmi, K., Keller, G., Steinmann, P., Matera, V., Berner, Z., Stüben, D., 2007. Phosphorus and the roles of productivity and nutrient recycling during Oceanic Anoxic Event 2. Geology 35, 483–486.

Negra, M.H., Zagrarni, M.F., Hanini, A., Strasser, A., 2011. The filament event near the Cenomanian-Turonian boundary in Tunisia: filament origin and environmental signification. Bulletin de la Société Géologique de France,182(6), 507–519.

Núñez-Useche, F., Barragán, R., Moreno-Bedmar, J.A., Canet, C., 2015. Geochemical and paleoenvironmental record of the early to early late Aptian major episodes of accelerated change: Evidence from Sierra del Rosario, Northeast Mexico. Sedimentary Geology, 324, 47–66.

Ohmoto, H., Kaiser, C.J., Geer, A., 1990. Systematics of sulphur isotopes in recent marine sediments and ancient sediment-hosted base metal deposits. In: Herbert, H.K., Ho, S.E. (Eds.), Stable isotopes and fluid processes in mineralization. University of Western Australia Publ. 23, 70–120.

Passier, H.F., Middelburg, J.J., de Lange, G.J., Böttcher, M.E., 1997. Pyrite contents, microtextures, and sulfur isotopes in relation to formation of the youngest eastern Mediterranean sapropel. Geology 25, 519–522.

Paytan, A., Kastner, M., Campbell, D., Thiemens, M.H., 2004. Seawater sulfur isotope fluctuations in the Cretaceous. Science 304, 1663–1665.

Premoli Silva, I., Sliter, W.V., 2002. Practical manual of Cretaceous planktonic foraminifera. In: Premoli Silva, I., Rettori, R. (Eds.), *International School on Planktonic Foraminifera, 1st Course*. University of Perugia, Italy, p. 462.

Poulton, S.W., Henkel, S., März, C., Urquhart, H., Flögel, S., Kasten, S., Jaap, S., Sinninghe, S., Wagner, T., 2015. A continental-weathering control on orbitally driven redox-nutrient cycling during Cretaceous Oceanic Anoxic Event 2. Geology, 43(11), 963–966.

Reitz, A., Pfeifer, K., de Lange, G.J., Klump, J., 2004. Biogenic barium and the detrital Ba/Al ratio: a comparison of their direct and indirect determination. Marine Geology 204, 289–300.

Reolid, M., Nagy, J., Rodríguez-Tovar, F. J., 2010. Ecostratigraphic trends of Jurassic agglutinated foraminiferal assemblages as a response to sea-level changes in shelf deposits of Svalbard (Norway). Palaeogeography, Palaeoclimatology, Palaeoecology, 293(1), 184–196.

Reolid, M., Sánchez-Quiñónez, C.A., Alegret, L., Molina, E., 2015. Palaeoenvironmental turnover across the Cenomanian-Turonian transition in Oued Bahloul, Tunisia: foraminifera and geochemical proxies.Palaeogeography, Palaeoclimatology, Palaeoecology, 417, 491–510.

Rickard, D., 2012. Sulfidic sediments and sedimentary rocks. In: Van Loon, A.J. (Ed.), Developments in Sedimentology. Elsevier, p. 801.

Rigual-Hernández, A.S., Sierro, F.J., Bárcena, M.A., Flores, J.A., Heussner, S., 2012. Seasonal and interannual changes of planktic foraminiferal fluxes in the Gulf of Lions (NW Mediterranean) and their implications for paleoceanographic studies: Two 12-year sediment trap records.Deep Sea Research Part I: Oceanographic Research Papers, 66, 26–40.

Robaszynski, F., Zagrarni, M.F., Caron, M., Amédro, F., 2010. The global bio-events at the Cenomanian-Turonian transition in the reduced Bahloul Formation of Bou Ghanem (central Tunisia). Cretaceous Research 31, 1–15.

Schlanger, S.O., Jenkyns, H.C., 1976. Cretaceous oceanic anoxic events—causes and consequences. Geologie en Mijnbouw 55, 179–184.

Salmon, K. H., Anand, P., Sexton, P.F., Conte, M., 2014. Upper ocean mixing controls the seasonality of planktonic foraminifer fluxes and associated strength of the carbonate pump in the oligotrophic North Atlantic.Biogeosciences Discussions 11, 12223–12254.

Snow, L., Duncan, R.A., 2001. Hydrothermal links between ocean plateau formation and global anoxia, *Eos Trans. AGU, 82*(47), Fall Meet. Suppl., abstract OS41A-0437.

Snow, L.J., Duncan R.A., Bralower T.J., 2005. Trace element abundances in the Rock Canyon Anticline, Pueblo, Colorado, marine sedimentary section and their relationship to Caribbean plateau construction and oxygen anoxic event 2. Paleoceanography 20, PA3005.

Solari, L.A., Gómez-Tuena, A., Bernal, J.P., Pérez-Arvizu, O., Tanner, M., 2009. U-Pb Zircon Geochronology with an Integrated LA-ICP-MS Microanalytical Workstation: Achievements in Precision and Accuracy. Geostandards and Geoanalytical Research 34, 5–18.

Suter, M., 1984. Cordilleran deformation along the eastern edge of the Valles–San Luis Potosí carbonate platform, Sierra Madre Oriental fold-thrust belt, east-central Mexico. Geological Society of America Bulletin 95, 1387–1397.

Taylor, A.M., Goldring, R., 1993. Description and analysis of bioturbation and ichnofabric. Journal of the Geological Society of London 150, 141–148.

Trabucho Alexandre, J., Tuenter, E., Henstra, G.A., van der Zwan, K.J., van de Wal, R.S.W., Dijkstra, H.A., and de Boer, P.L., 2010. The mid-Cretaceous North Atlantic nutrient trap: Black shales and OAEs: Paleoceanography 25, PA4201.

Tribovillard, N., Algeo, T.J., Lyons, T., Riboulleau, A., 2006. Trace metals as paleoredox and paleoproductivity proxies: An update. Chemical Geology 232, 12–32.

Twichell, S.C., Meyers, P.A., Diester-Haass, L., 2002. Significance of high C/N ratios in organic-carbon-rich Neogene sediments under the Benguela Current upwelling system. Organic Geochemistry 33, 715–722.

Uchman, A., Rodríguez-Tovar, F.J., Machaniec, E., Kędzierski, M., 2013. Ichnological characteristics of Late Cretaceous hemipelagic and pelagic sediments in a submarine high around the OAE-2 event: A case

from the Rybie section, Polish Carpathians. Palaeogeography, Palaeoclimatology, Palaeoecology, 370, 222–231.

Van Mooy, B.A.S., Keil, R.G., Devol, A.H., 2002. Impact of suboxia on sinking particulate organic carbon: Enhanced carbon flux and preferential degradation of amino acids via denitrification. Geochimica et Cosmochimica Acta 66, 457–465.

Wedepohl, K.H., 1971. Environmental influences on the chemical composition of shales and clays. Physics and Chemistry of the Earth 8, 305–333.

Westermann, S., Caron, M., Fiet, N., Fleitmann, D., Matera, V., Adatte, T., Föllmi, K.B., 2010. Evidence for oxic conditions during oceanic anoxic event 2 in the northern Tethyan pelagic realm. Cretaceous Research 31, 500-514.

Wignall, P.B., 1994. Black Shales. Geology and Geophysics Monographs 30. Oxford University Press, Oxford. 130 p.

Wignall, P.B., Hallam, A., 1991. Biofacies, stratigraphic distribution and depositional models of British onshore Jurassic black shales. Geological Society of London Special Publication 58, 291–309.

Wilkin, R.T., Barnes, H.L., Brantley, S.L., 1996. The size distribution of framboidal pyrite in modern sediments: An indicator of redox conditions. Geochimica et Cosmochimica Acta 60, 3897–3912.

Xu, G., Hannah, J.L., Bingen, B., Georgiev, S., Stein, H.J., 2012. Digestion methods for trace element measurements in shales: Paleoredox proxies examined. Chemical Geology, 324, 132–147.

FIGURE CAPTIONS

Fig. 1. (A) Paleoceanographic reconstruction of the Cenomanian–Turonian (http://jan.ucc.nau.edu/~rcb7/), showing the location of Mexico and the Xilitla section. (B). Central–northeastern portion of the Sierra Madre Oriental Fold-Thrust Belt with the major paleogeographic elements. (C) Schematic map of Xilitla.

Fig. 2. Lithology, facies (F1 to F3) and age distribution of the Xilitla section. Bentonite beds are green, and are wider than the other lithologies in order to make them stand out visually in the stratigraphic column. The right panel shows photomicrographs of the four indentified bioevents.

Fig. 3. LA-ICP-MS U–Pb analysis of zircons separated from bentonite sample Az, plotted on Tera–Wasserburg diagram. The TuffZirc age and best age are also plotted. See Fig. 2 for stratigraphic position of sample.

Fig. 4. Photographs illustrating the general characteristics of the outcrop: (A) Lower part of the Xilitla section (Quarry I). Several loose slabs of limestone can be observed in the front of the picture. (B) Notice the yellowish-reddish stains of some beds as a result of pyrite (*p*) weathering (Quarry III). (C) Layers of flint (*f*) with a pinch-and-swell structure (Pen size=12 cm). (D) Interbedded limestones and bentonites (*b*) (Quarry III). (E) Laminated limestone bed with laminae of greenish bentonite (*b*). (F) Alternation of dark gray laminated limestone with pyrite (p), and light-colored bioturbated limestone (bed 197).

Fig. 5. General characteristics of the sedimentary facies. Facies F1: (A) Limestone with undisrupted laminated fabric and pyrite as laminae (*l*) and nodules (*n*) (bed 115). (B) Laminae of pyrite (bed 22). (C) Sun pyrite (bed 35). (D) Disarticulated remains of fish (bed 95). (E) Fish scale (bed 6).

(F) Ammonite (bed 60). Facies F2: (G) Moderately bioturbated and laminated limestone. Pyrite is disseminated in bed-parallel burrows (*b*) and laminated (*l*) (bed 65). (H) Bedding-parallel burrows (bed 19) (Pen size=12 cm). (I) *Planolites* (bed 7) (Pen size=12 cm). (J) *Chondrites (bed 52)*. (K) *Inoceramus cicloides* Wegner. Note the fish scale (*f*) (bed 12). (L) *Inoceramus (Mytiloides) labiatus* Schlotheim (bed 126). (M) Ripple marks caused by currents on the upper bed surface (top view, bed 18). Facies F3: (N) Bioturbated limestone with a LOD pattern. Small *Chondrites* (*Ch*) and large *Zoophycos*–like (*Zo*) (bed 207). (O). DOL bioturbated pattern. Note different cutting relationships between bioturbation and vertical burrows (*v*) (bed 212). (P) DOL bioturbated pattern. From bottom to top, there is an increase in bioturbation intensity (bed 205). (Q) Vertical mid-strata burrows (bed 108). See the position of beds in Fig. 2.

Fig. 6. Microscopic characteristics of the sedimentary facies. Facies F1: (A) Wackestone with planar laminated matrix and planktic foraminifera (bed 12). (B) Remains of fish (*f*) and planktic foraminifera in a wackestone with anisotropic fabric (bed 199). (C) Bivalve shell fragment (bed 30). (D) Authigenic glauconite (*g*) as cement and within planktic foraminifera (bed 161). (E) Subfacies F1B. Occasional radiolarian wackestone/packstone facies with no evidence of bioturbation (bed 87). Facies F2: (F) Disrupted lamination by horizontal–sub horizontal burrows (bed 204). (G) Bedding–parallel burrows (186). Facies F3: (H) Benthic foraminifera (*b*) in bioturbated facies (bed 50). (I) Vertical burrow filled with mudstone-type sediment (bed 80). See the position of beds in Fig. 2.

Fig. 7. Microscopic features of framboidal pyrite from the Xilitla section. Photomicrographs under reflected light microscope: (A) Massive (m) and framboidal (f) pyrite (bed 30). (B) Pyrite framboids in the calcareous matrix (bed 152). Photomicrographs under scanning electron microscope: (C) Framboids with disordered structure composed of randomly aggregated irregular microcrystals. In the center there is a framboid with hexagonal arrangement made up of

octahedral microcrystals, all of which share a common morphological orientation (arrow) (bed 17). (D) Close–up of microcrystals of a framboid on the right in C. Note spherical clusters of poorly-formed octahedral particles. (E) Framboid with hexagonal arrangement, composed of octahedral microcrystals with slight truncation and totally disoriented (bed 22). (F) To the left, there is a framboid with cubo–octahedral microcrystals in hexagonal arrangement and almost perfect orientation (bed 126).

Fig. 8. Framboidal pyrite plots: (A) Stratigraphic distribution, diameter and content of framboidal pyrite. (B) Mean versus standard deviation plot of framboidal pyrite. The boundary between fields for euxinic, anoxic and dysoxic environments is that seen in modern depositional settings (from Wilkin et al., 1996). Size of circles is proportional to the estimated content of framboids. The color of the dots represents the sedimentary facies.

Fig. 9. Correlation of bioevents and carbon isotope events across the Cenomanian–Turonian transition between the Xilitla section (Mexico), and sections in Colorado-USA, Central Tunisia and Tibet-China. Notice that the $\delta^{13}C$ data from the Xilitla section do not record the typical features of the globally documented Cenomanian–Turonian positive excursion.

Fig. 10. Vertical profiles of TOC (%), TOC/N_{TOT}, S_{TOT} (%), Al-normalized RSTEs and Ba_{bio} (ppm) of the Xilitla section. The values with asterisk in the Al-normalized profiles represent concentrations of each corresponding normalized element in the average shale (AS) from Wedepohl (1971).

Fig. 11. Rock Eval data. Hydrogen index (HI) *vs*. oxygen index. Maturation paths shown for type I – II–III organic matter (modified pseudo-van Krevelen diagram, Tisot and Welte, 1984). Each sample is identified by the corresponding bed number.

Fig. 12. Calculated enrichment factors (EFs; note logarithmic scale) for RSTE measured in the Xilitla section. All measurements (white box-plot) and lowest 9 m values (light grey box-plot) are compared to the mean of the Cenomanian–Turonian (C–T) black shales from various locations by Brumsack (2006) (black box-plot). The line in the middle of the boxes is plotted at the median, and "x" represents the mean. The horizontal dashed line indicates the value for which there is no enrichment/depletion with regards to average shale composition.

Fig. 13. Results of EDS analysis on pyrite framboids (A) Scanning electron micrograph of pyrite framboids. Note the dark matrix between microcrystals and surrounding the framboids (arrows). (B) Enlarged image of the boxed area in (A). EDS analysis on the internal matrix (C) and a single microcrystal (D) shows that carbon is present in the former. Both analyzed areas are shown by arrows in (B).

Fig. 14. The evolution of the $\delta^{34}S_{py}$ observed in the Xilitla section compared to that from Site 158, Portland Core and Core S57.

Fig. 15. Proposed model of bottom-water conditions during the deposition of the Agua Nueva Formation at Xilitla. The position of the oxic-anoxic interface in regards to the sediment-water interface determined the variations between anoxic to dysoxic and oxic bottom-water conditions.
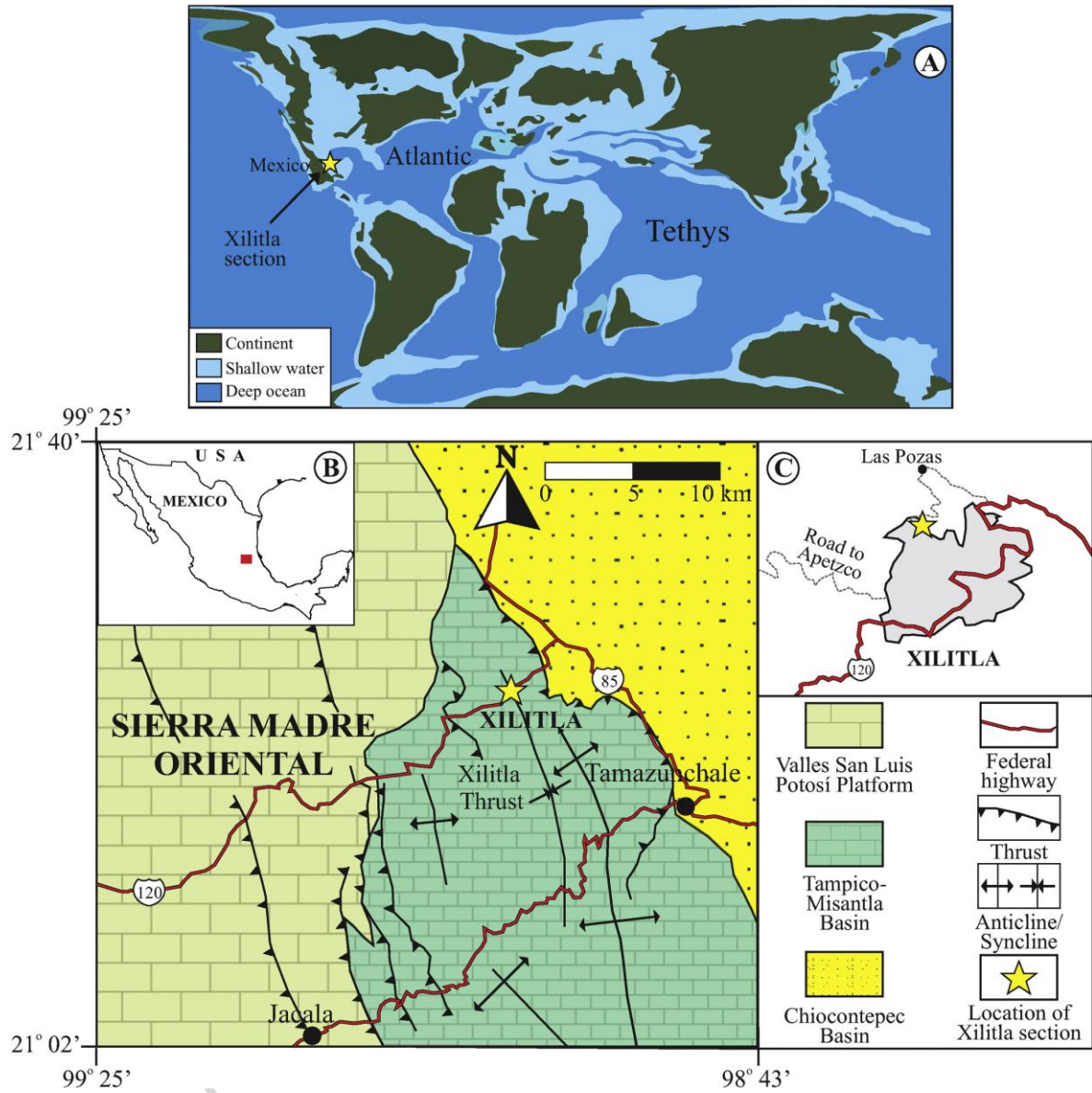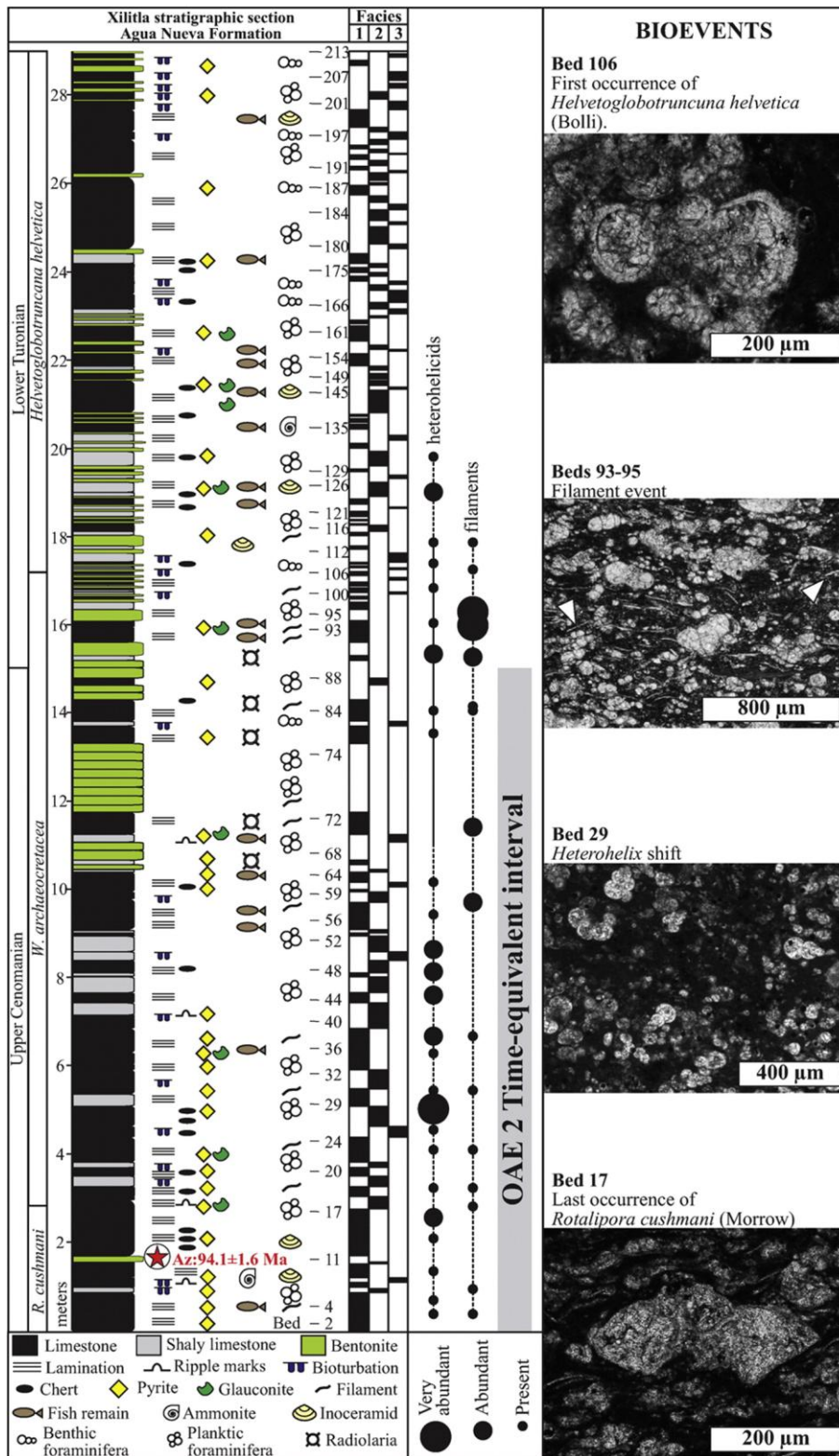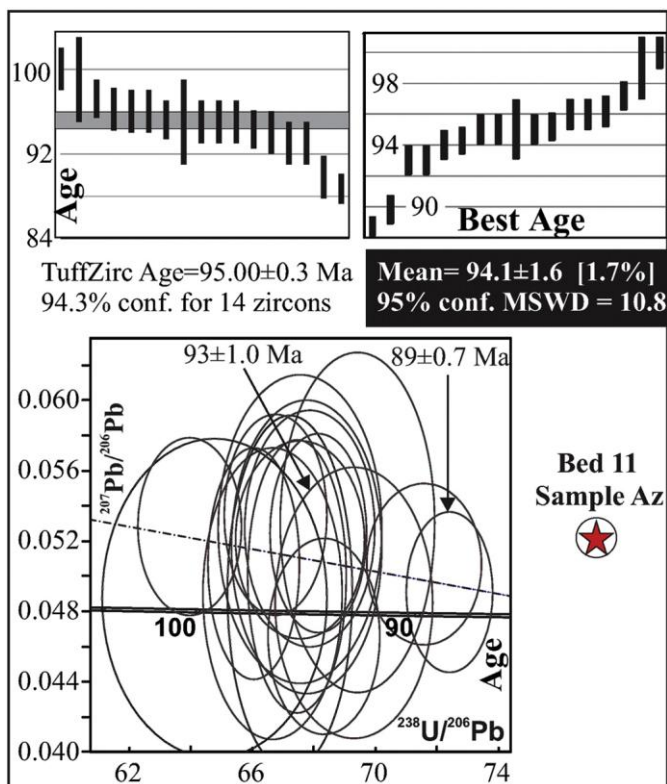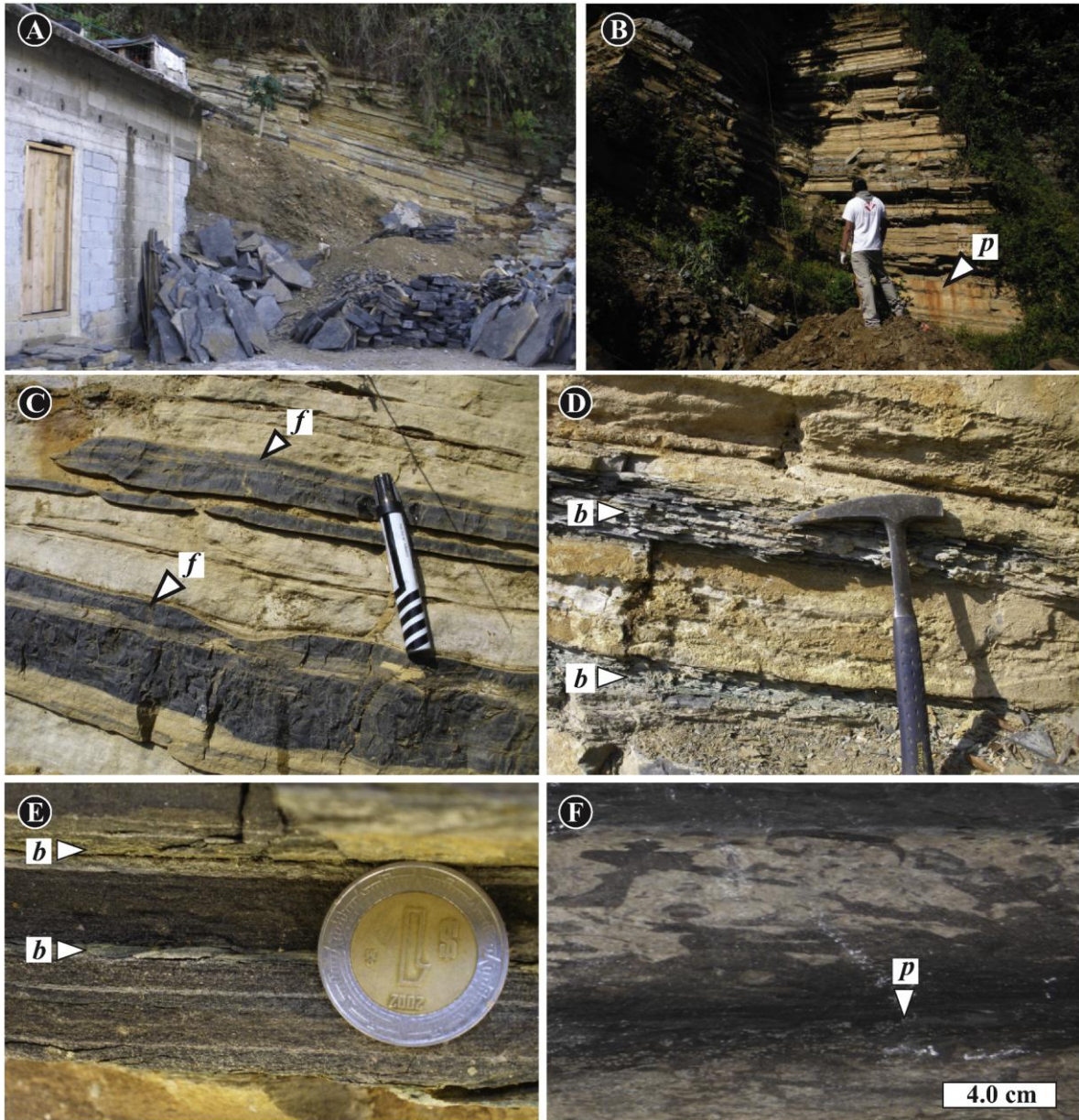
Figure 1

Figure 2

Figure 3

Figure 4
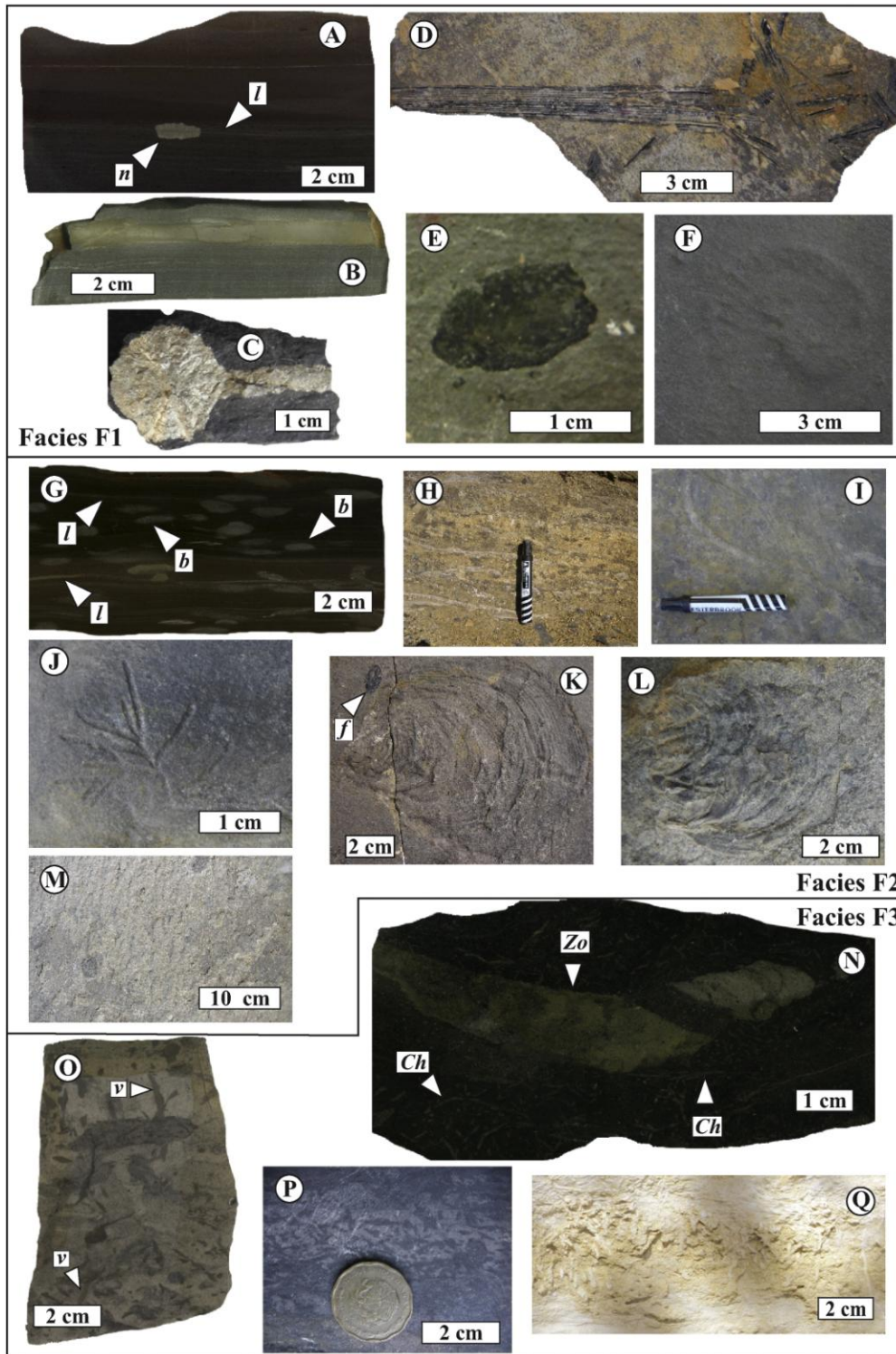
Figure 5
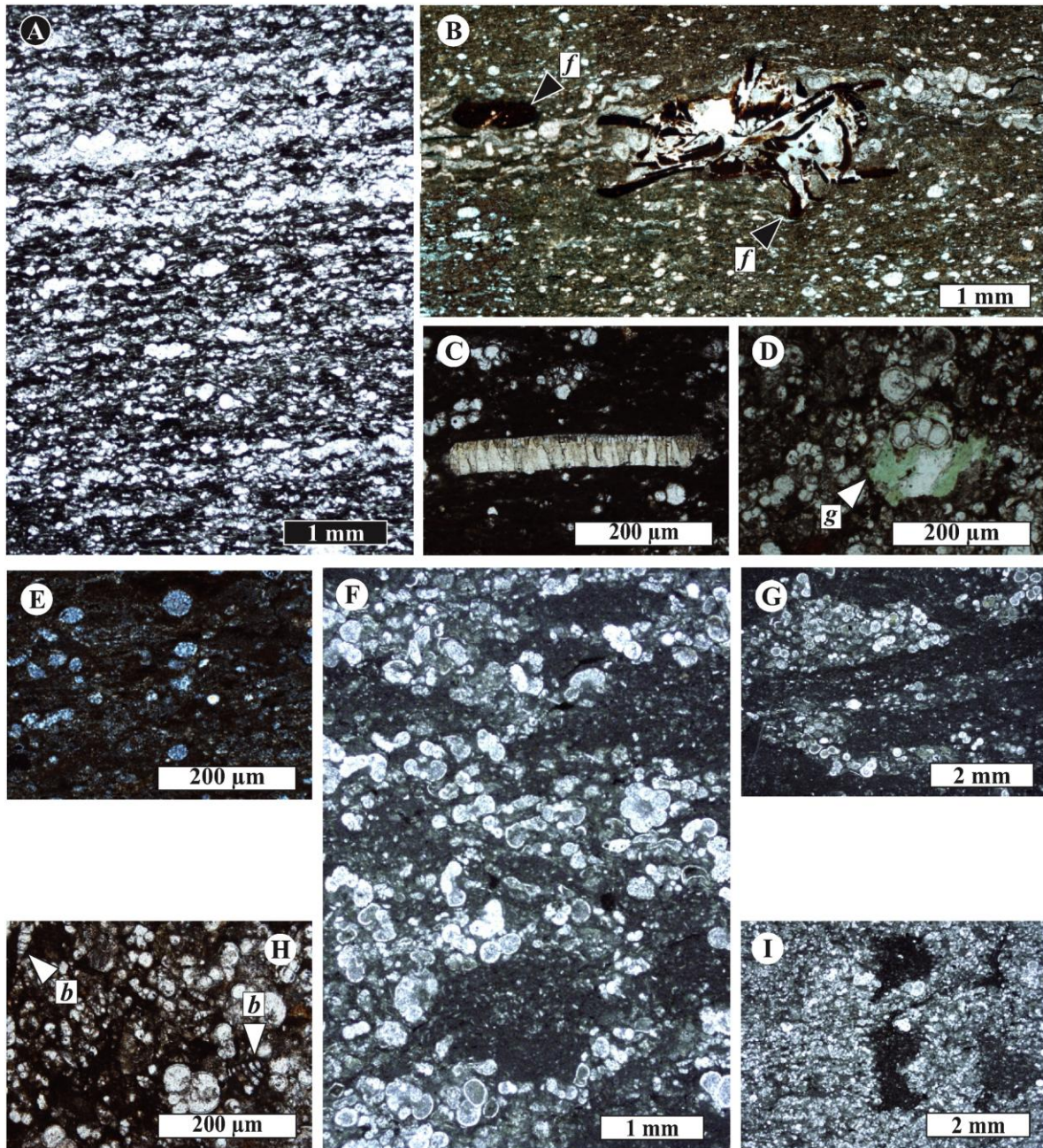
Figure 6
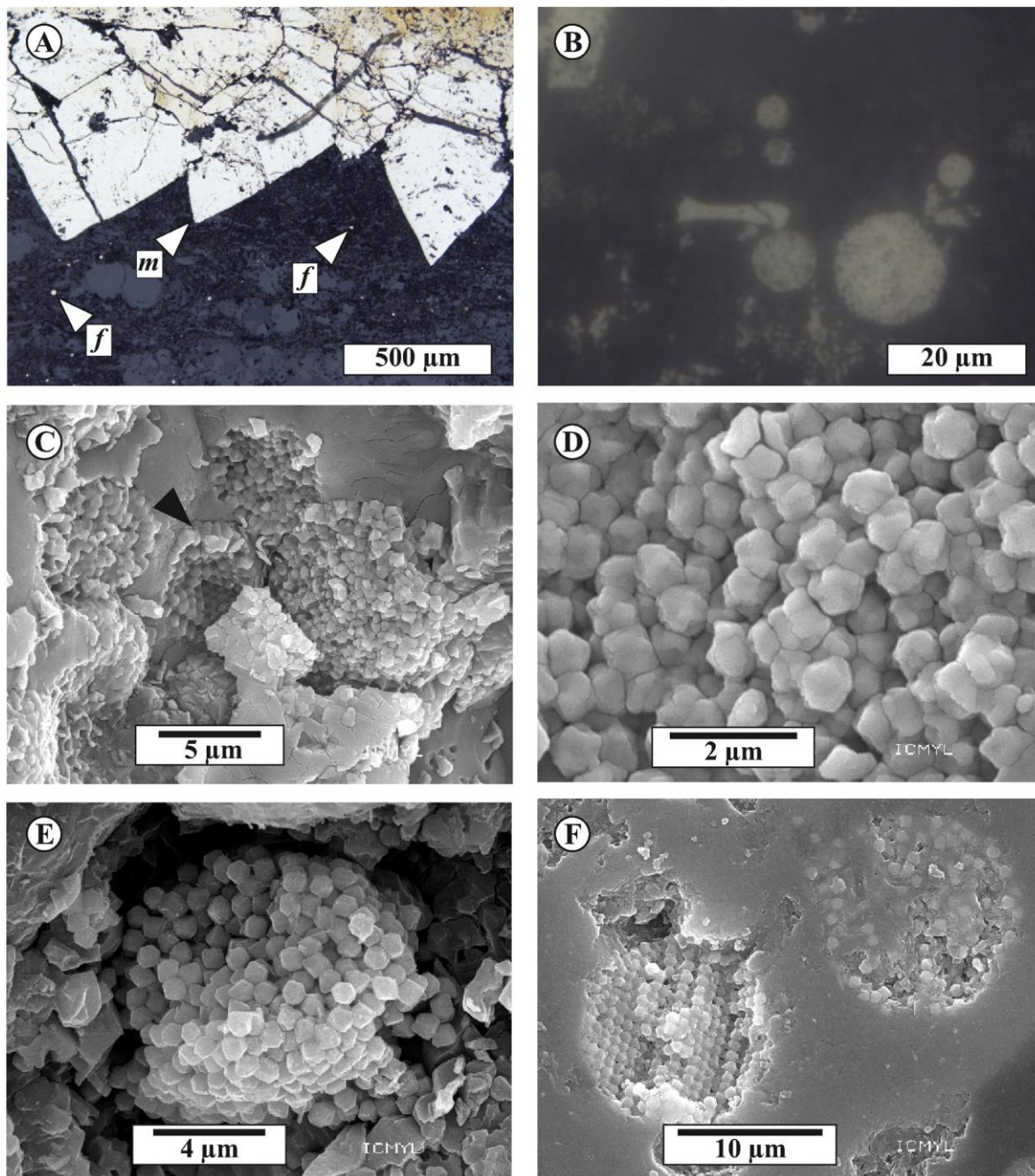
Figure 7
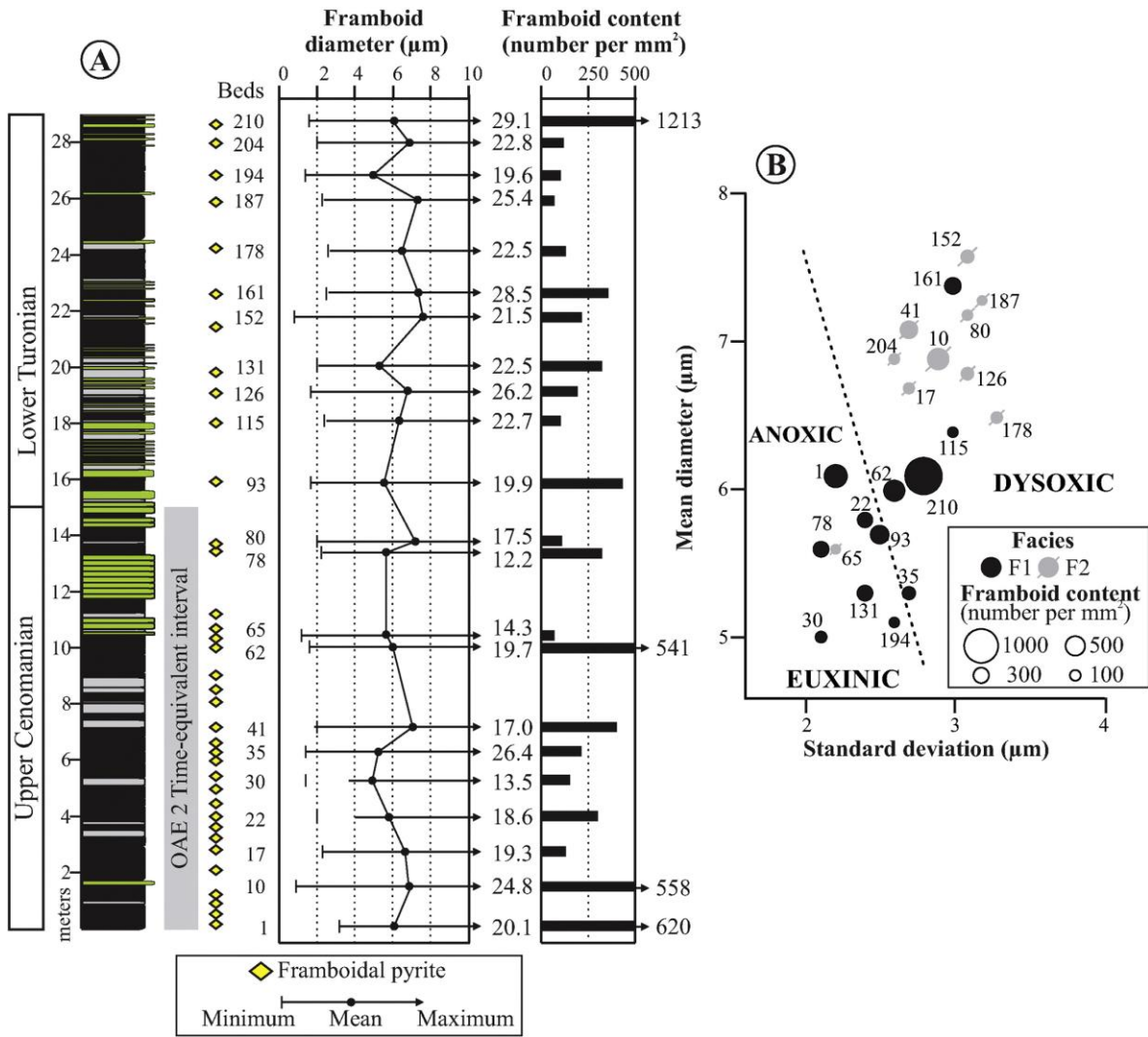
Figure 8
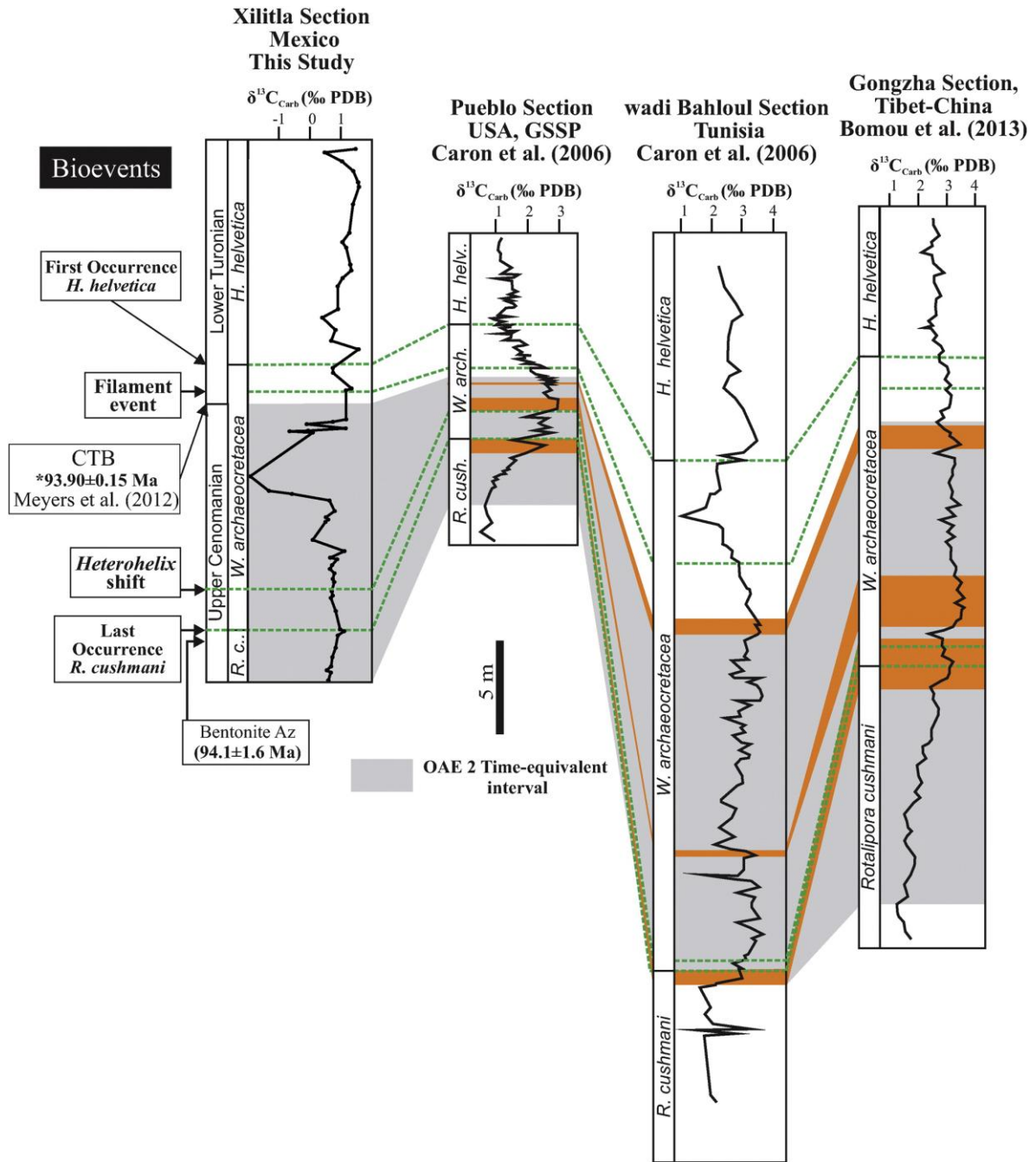
Figure 9
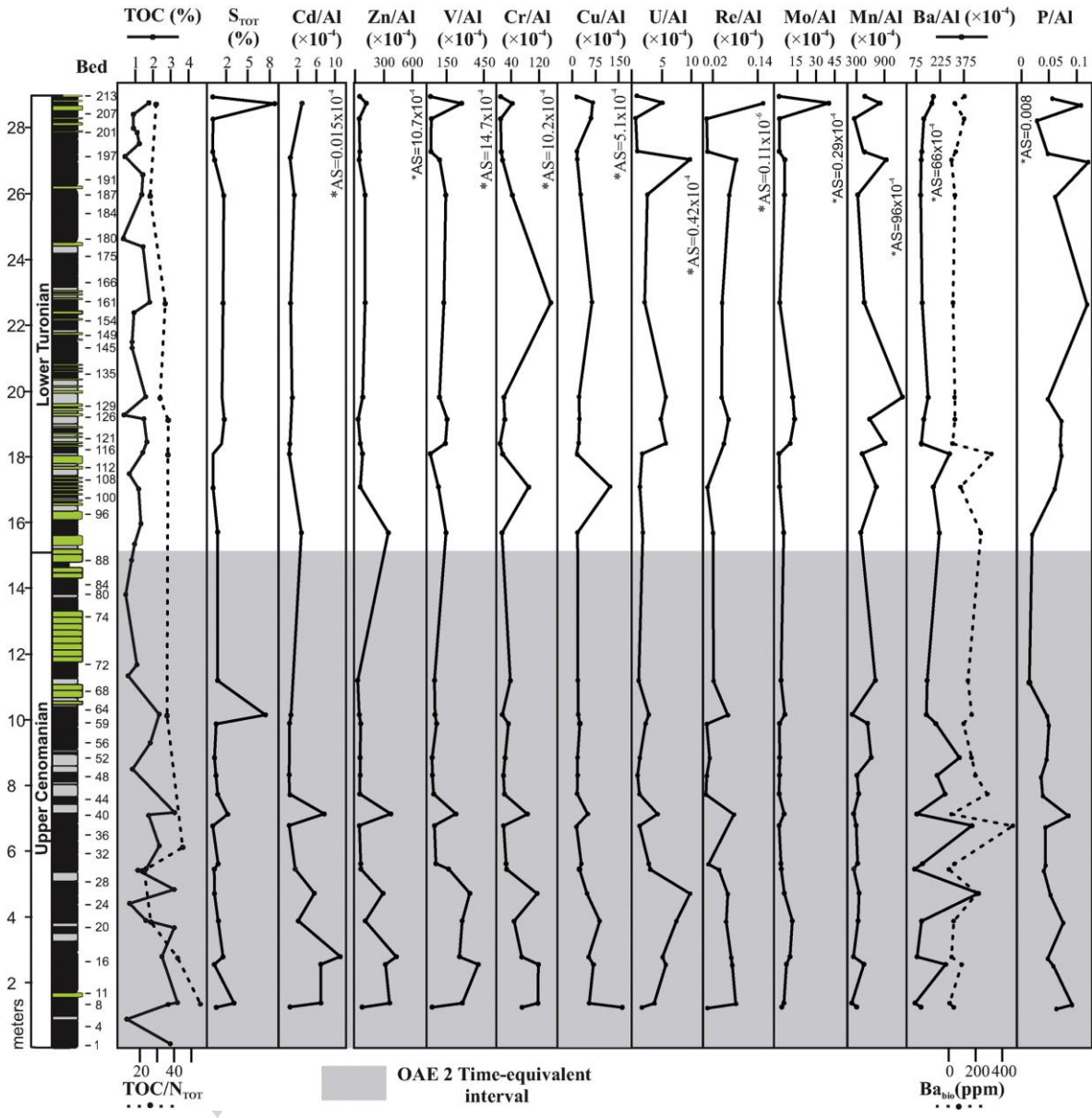
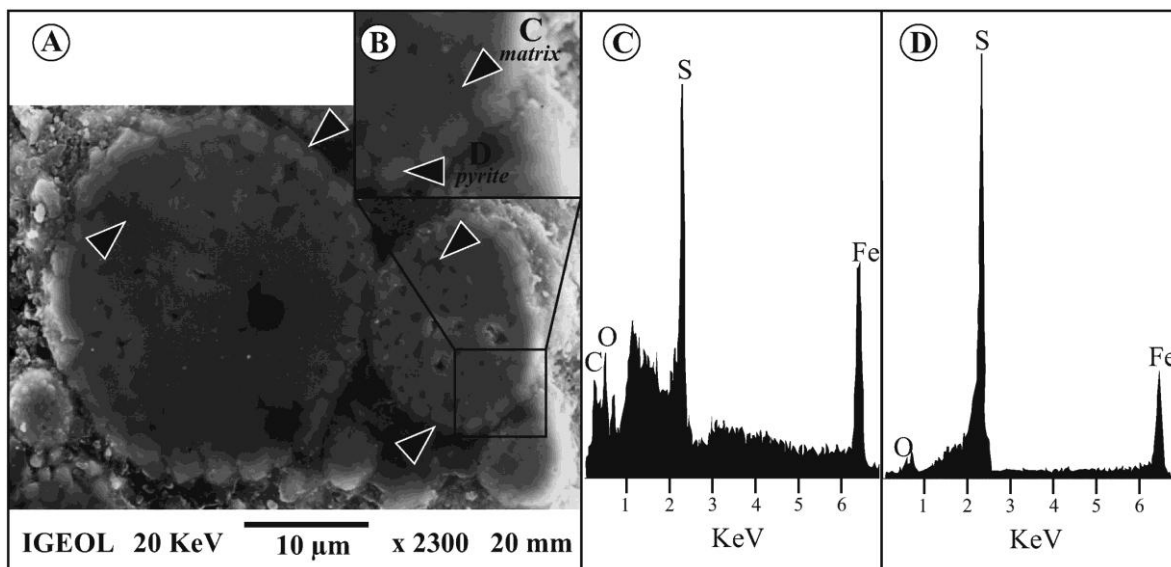**Figure 10**
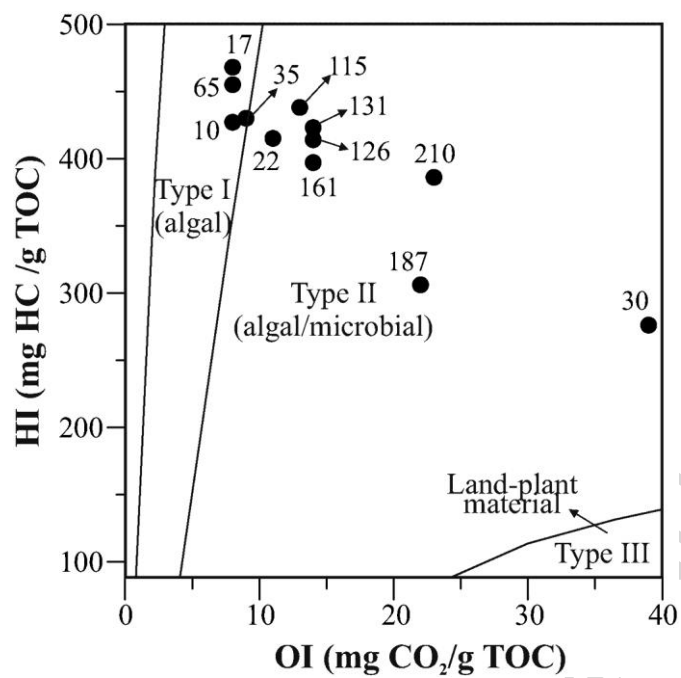
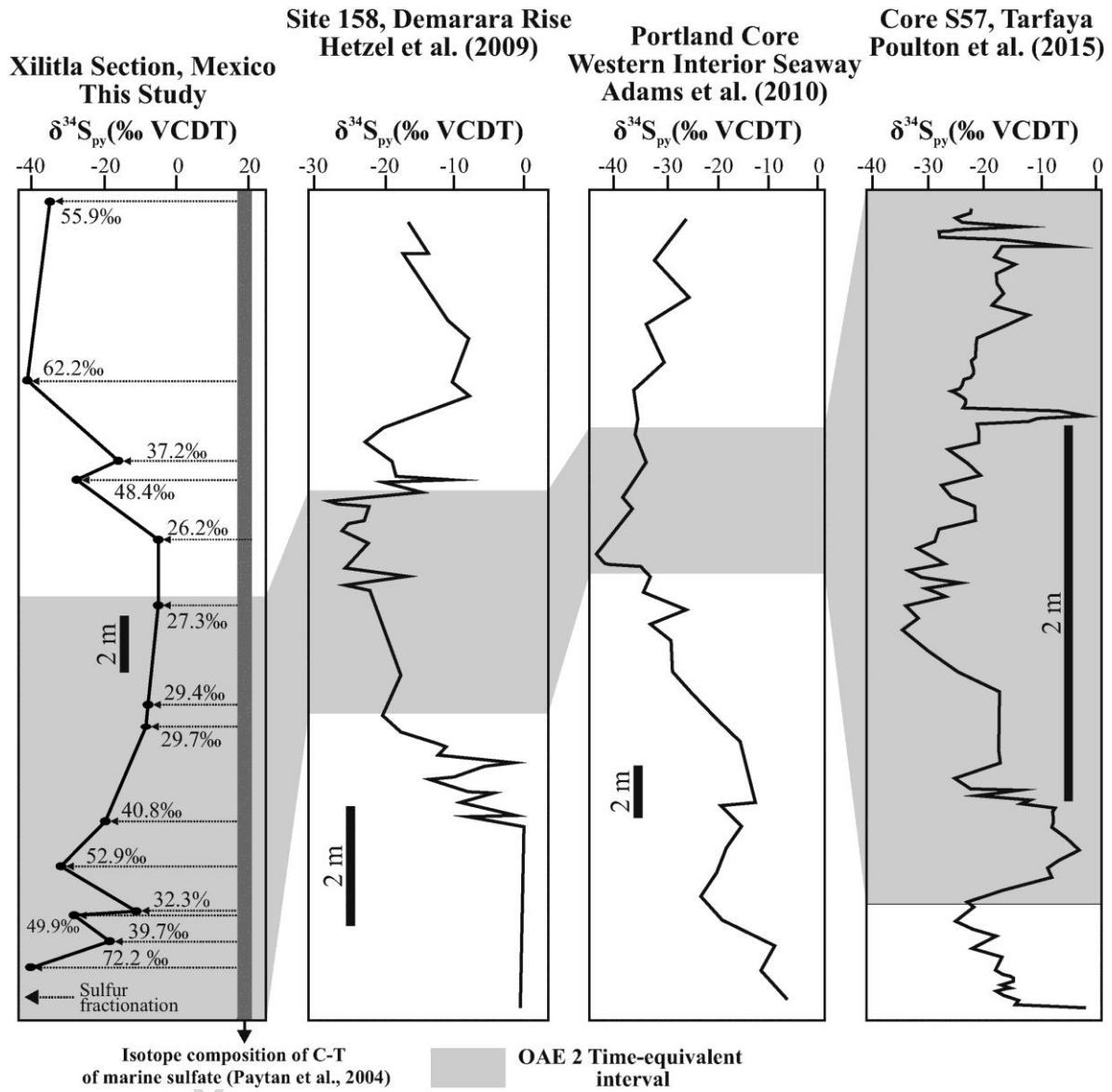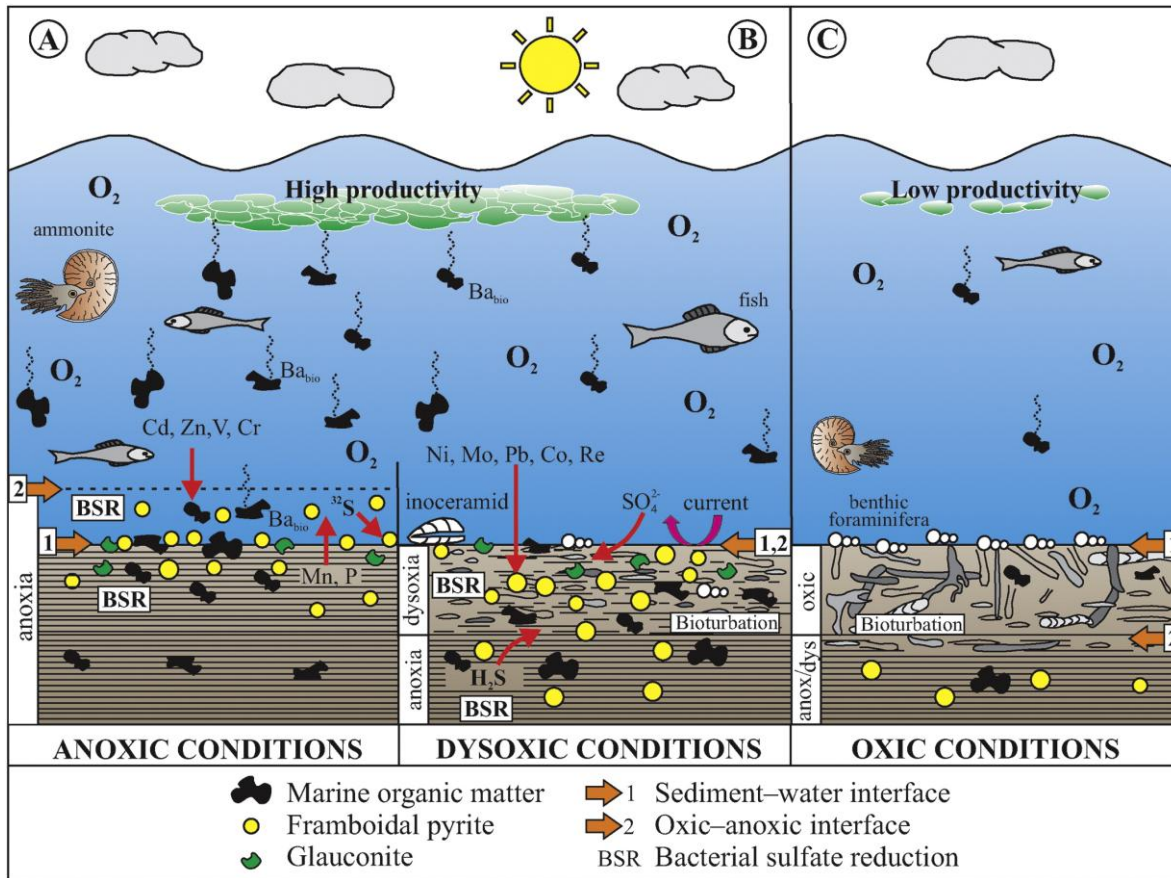**Figure 11**
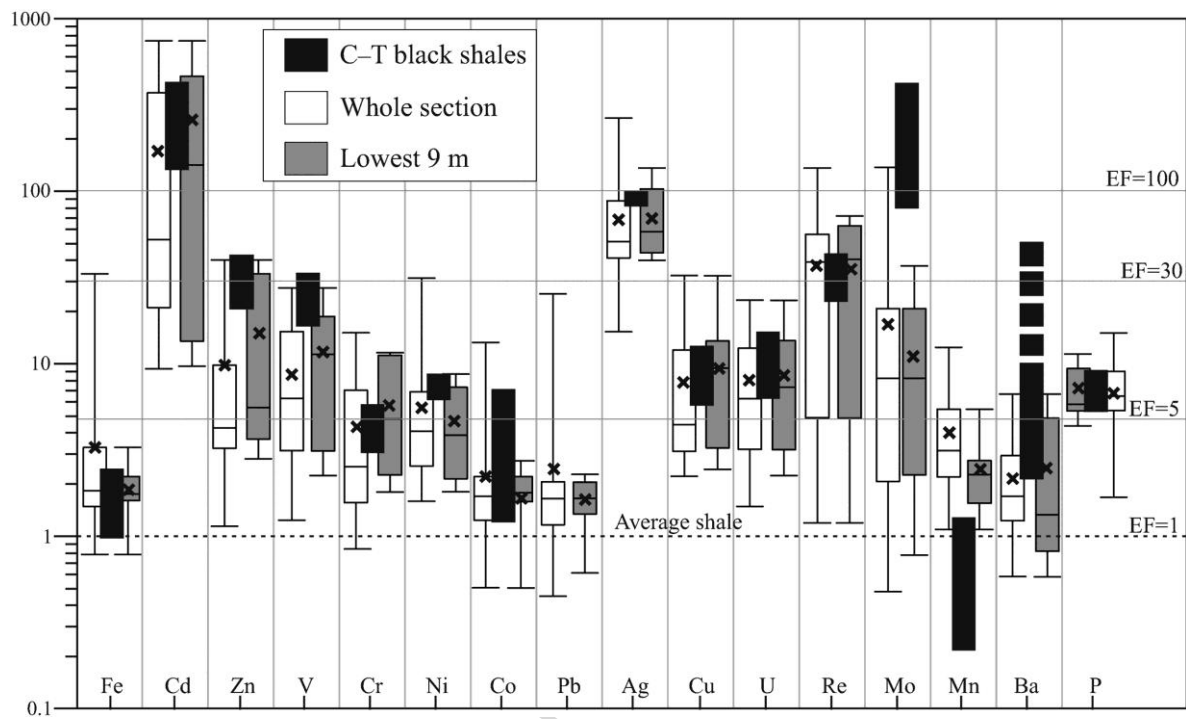
Figure 12

Figure 13

Figure 14

Figure 15

Table 1. Pyrite framboid size statistical parameters. N= number of framboids in measured area, Min. F.D.= Minimum framboid diameter measured under optical microscope, Min. F.D. SEM= Minimum framboid diameter measured under SEM, Max. F.D.= Maximum framboid diameter measured under optical microscope. Underestimation of smallest framboids under reflected light affecting the calculated relative content can be ruled out, because minimum framboid size estimated by SEM is similar to the minimum size determined with the optical microscope.

Bed	Facies	Mean (µm)	S.D.	Min F.D. (µm)	Min F.D. SEM (µm)	Max F.D. (µm)	Framboid content (number per mm^2)
210	1	6.1	2.8	1.6	1.8	29.1	1213
204	2	6.9	2.6	2.0	-	22.8	115
194	1	5.1	2.6	1.4	1.4	19.6	99
187	2	7.3	3.2	2.3	2.5	25.4	70
178	2	6.5	3.3	2.6	-	22.5	150
161	1	7.4	3.0	2.5	2.5	28.5	355
152	2	7.6	3.1	0.8	1.0	21.5	214
131	1	5.3	2.4	2.0	2.1	22.5	318
126	2	6.8	3.1	1.7	1.7	26.2	192
115	1	6.4	3.0	2.4	2.5	22.7	102
93	1	5.7	2.5	1.7	-	19.9	432
80	2	7.2	3.1	2.0	-	17.5	110
78	1	5.6	2.1	2.2	2.4	12.2	320
65	2	5.6	2.2	1.2	1.5	14.3	70
62	1	6.0	2.6	1.6	1.9	19.7	541
41	2	7.1	2.7	2.0	2.4	17.0	397
35	1	5.3	2.7	1.4	1.8	26.4	211
30	1	5.0	2.1	1.4	2.1	13.5	150
22	1	5.8	2.4	2.0	2.6	18.6	300
17	2	6.7	2.7	2.3	2.3	19.3	130
10	2	6.9	2.9	0.9	1.1	24.8	558
1	1	6.1	2.2	3.2	3.2	20.1	620

Table 2. Chemical composition of pyrite in the analyzed samples (WDS analysis data).

Bed	Pyrite Texture	S	Fe	V	Ni	Th	Mo	U	Total	S	Fe	V	Ni	Th	Mo	U
					wt. (%)								(ppm)			
210	Framboid	53.159	45.732	-	0.017	-	0.451	-	99.359	531590	457320	-	170	-	4510	-
210	Laminated	53.303	46.636	-	-	-	0.524	0.015	100.478	533030	466360	-	-	-	5240	300
161	Framboid	53.147	46.311	0.29	0.034	0.017	0.498	0.013	100.31	531470	463110	5800	340	170	4980	260
126	Framboid	52.905	47.084	-	0.015	0.043	0.591	0.011	100.649	529050	470840	-	150	430	5910	220
126	Laminated	52.681	46.176	-	0.038	0.006	0.541	0.114	99.556	526810	461760	-	380	60	5410	2280
30	Framboid	52.668	46.293	-	0.034	-	0.471	-	99.466	526680	462930	-	340	-	4710	-
22	Framboid	54.028	47.385	-	-	0.114	0.524	-	102.051	540280	473850	-	-	1140	5240	-
22	Laminated	54.019	46.986	-	0.016	-	0.568	0.042	101.631	540190	469860	-	160	-	5680	840

Table 3. Correlation coefficients (R) between Al-normalized trace elements and TOC- S_{TOT}.

Trace Element/Al	TOC R (n=19)	S_{TOT} R (n=29)	Trace Element	TOC R (n=19)	S_{TOT} R (n=29)
Fe/Al	0.05	0.8	Ag/Al	0.17	0.50
Cd/Al	0.72	0.08	C/Al	0.23	0.04
Zn/Al	0.68	0.09	U/Al	0.38	0.14
V/Al	0.67	0.24	Re/Al	0.45	0.67
Cr/Al	0.61	0.04	Mo/Al	0.06	0.72
Ni/Al	0.16	0.73	Mn/Al	-0.43	0.03
Co/Al	0.06	0.67	Ba/Al	0.15	0.21
Pb/Al	0.02	0.68	P/Al	0.28	0.33

66

Highlights

- We documented the biotic turnover and oxygen depletion associated with OAE 2.

- First record of the filament event and the *Heterohelix* shift from Mexico

- This study constructs a model by integrating sedimentary, biological and geochemical data.

- A global mechanism driving the global sedimentary sulfur isotope signal during the OAE 2.